Water Weakening and Temperature Effects on the Deformation and Transport Properties of Indiana Limestone

Katherine Watter

Advisor: Dr. Wen-lu Zhu

29 April 2011

GEOL394H

Table of Contents

Abstract

When subject to an applied stress or change in pore pressure, a rock will respond with either a compaction or dilation of pore space, consequently affecting fluid transport properties such as porosity and permeability. The observed deformation depends upon rock composition; silicate-based rocks such as sandstones and granites will follow a different deformation path than calcite-based rocks such as limestones. Calcite requires lower shear stresses to initiate twinning and dislocation slip relative to quartz (Vajdova et al., 2004a); this difference leads to radically different types of deformation. The means to understand and predict the occurrence and degree of deformation is based on a fundamental understanding of the failure mode, inelastic behavior, and brittle-ductile transition. Indiana limestone is the focus of our experiment because its near compositional homogeneity (97% calcite) makes it an excellent specimen in which to observe calcite deformation behavior. We hypothesize that crystal plasticity plays an important role in the deformation behavior of Indiana Limestone. Further, we hypothesize that as temperature increases, crystal plasticity will be more pronounced. To test these hypotheses, transport property evolution via calcite deformation in Indiana Limestone samples are observed during hydrostatic and triaxial deformation experiments at different temperature conditions. Qualitative and quantitative microstructural observations of deformed samples detect for evidence of crystal plasticity. Point counts in thin sections of deformed cores detect for twinning, a characteristic property of crystal plasticity, while some deformed cores exhibit macroscopic damage indicating the presence of plastic deformation. Previous deformation experiments on Indiana Limestone have been conducted by Vajdova et al. Our data follows, showing stiffer elastic modulii and greater reduction in permeability in high-temperature samples and, additionally, shows a weakening effect of water saturation on core deformation.

1.1 Introduction

Transport properties such as porosity and permeability exert control of fluid flow. Effective stress, the difference between the total stress acting on a substance and the pore pressure acting in the opposite direction, increases as a substance is drawn from the ground. For example, the extraction of hydrocarbon and groundwater resources reduces pore pressure, causing an increase in the effective stress of the reservoir or aquifer. For highly porous formations, this increase in effective stress may be enough to cause inelastic deformation (Vajdova et al., 2004a). Porosity, the ratio of pore volume to total volume in a rock and permeability, an intrinsic physical property of a rock that measures its ability to transmit fluid, are affected when exposed to dynamic environments where there are changes in pressure and temperature (Freeze and Cherry, 1979). An applied stress or change in pore pressure will cause a rock to respond with either a compaction or dilation of pore space. An understanding of compactant and dilatant behavior in addition to failure mode can be determined from the analysis of deformed rock samples such as measuring changes in porosity and permeability as well as calculating elastic modulii. Microstructural observation of deformed samples provides insight to more detailed deformation behavior, including whether evidence of crystal plasticity is apparent. The study of transport property evolution and deformation behavior has direct implications for geological industry. Eventually, research results can be used to form guidelines and constraints for the construction of a rock behavior model. Companies in industry can use these guidelines to

provide optimal working and operating methods based on local conditions and changing environments.

1.2 Deformation Mechanisms

Previous studies on sandstones, granites and limestones observe their respective deformation paths. Although the deformation behavior of quartz-based rocks has been widely studied, a deeper understanding of calcite-based rock deformation behavior is needed because stress-induced inelastic behavior is significantly different in low (<1%) and high (>5%) porosity rocks (Zhu and Wong, 1997). The compressibility of a rock is dependent not only on lithology, but also the porosity and grain size of a rock; for example, limestones are seen to be less compressible compared with sandstones of comparable porosities (Vajdova et al., 2004a). For porous siliciclastic rocks such as quartz, observations of permeability reduction accompanied with pore space dilation have been noted as the rock is stressed to brittle failure; there is a negative correlation between porosity and permeability. Generally, in low-porosity crystalline rocks such as limestones and shales, permeability enhancement is observed during dilatancy; there is a positive correlation between porosity and permeability (Wong and Zhu, 1999).

Compaction due to pore space collapse and dilatancy, which is induced by microcracking, are characteristic of brittle deformation. Post-deformational observations of Indiana Limestone show that grain crushing and cracking is responsible for a drastic change of physical characteristics in the rock (Fig 1). Pore space (black) between pre- and post-deformational cores drastically alters shape and size (Fig. 1, left to right). Stress applied on the sample promotes pore space collapse, subsequently causing grains to collide into each other. After pore collapse, microcracking is induced and the grain fractures into several smaller grains. Consequently, the rock now behaves as a lower-porosity rock and incurs an "over-consolidation" compacting stage where these smaller grains then fill in the initial pore space.

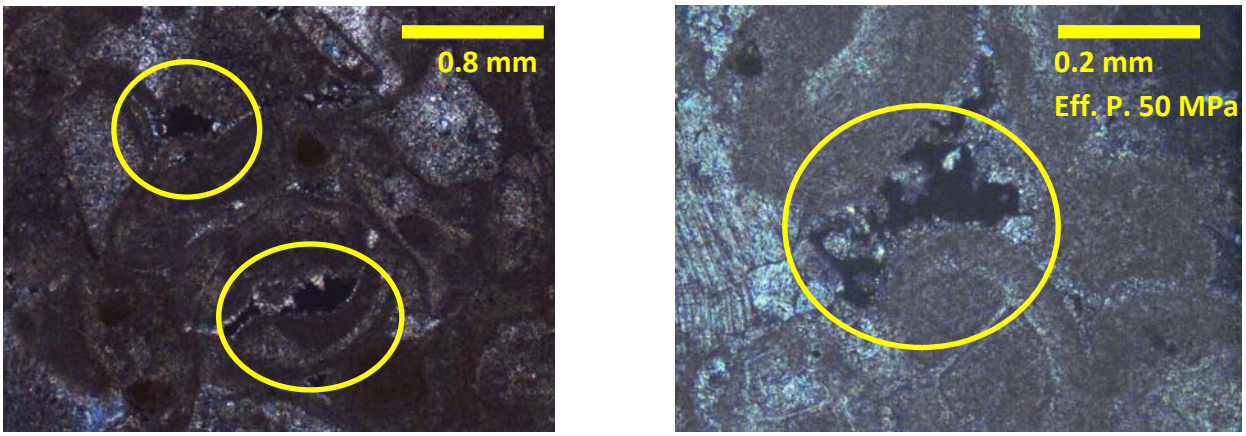

Fig. 1: Left: initial conditions, undeformed Indiana Limestone. Right: pore space collapse due to compaction and the subsequent microcracks in the grains. Microcracking breaks the grains into several smaller grains which then fill in the initial pore space. Porosity and permeability are affected.

Deformation may be elastic or inelastic. During elastic deformation, all energy stored in a material is released when an applied stress is removed. Inelastic deformation is non-recoverable and is further divided into brittle and ductile (plastic) deformation. Brittle deformation comprises

cataclastic flow and dilatancy, whereas crystal plasticity is characteristic of plastic deformation. Crystal plasticity has two components, mechanical twinning and dislocation slip.

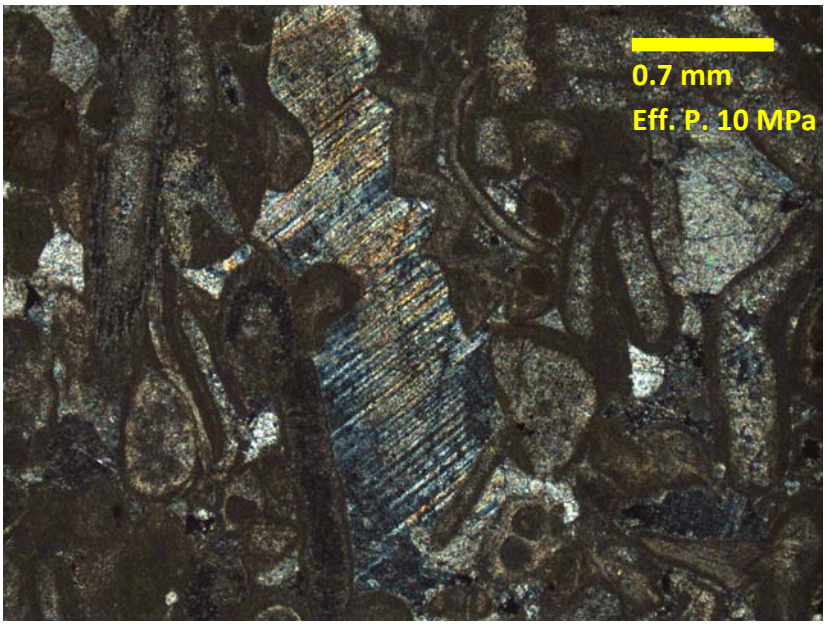

Fig. 2: Example of plastic deformation in Indiana Limestone. Twinning, seen in the center grain, is characteristic of crystal plasticity.

Observations of plastic deformation behavior indicate that twinning dominates in more porous limestones, whereas dislocation slip is activated in more compact limestones. Dislocation slip is thermally activated; if plastic failure in compact limestones arises from dislocation slip, there is evidence that the yield stress is dependent on temperature. Another factor to consider is the grain size of the sample. Indiana limestone has a relatively large grain size, ranging between 0.15 and 1 mm and porosity ranging from 13% to 20% (Frew et al, 2010). Limestone of any porosity may undergo a transition from brittle to plastic deformation at temperatures and pressures attainable in the laboratory; this is not true for quartz-based rocks because calcite requires lower shear stresses to initiate mechanical twinning and dislocation slip relative to quartz (Vajdova et al., 2004a).

As confining pressure increases, brittle fracture is inhibited and rocks fail via cataclastic flow (Zhu, 2006). Cataclastic flow is a term which describes permanent deformation achieved by the combination of microcracking, where the rock material is broken into fragments, and the relative movement of those fragments (Paterson, 1978). Friction between the moving fragments and the accompanying changes in porosity of the sample are important properties of cataclastic flow. Because confining pressure directly contributes to the amount of friction experienced, sample resistance to cataclastic flow is dependent on pressure. The type of cataclastic flow depends upon the initial porosity of the rock. Internal cracking and rearrangements promote dilatancy if the sample has a low initial porosity. Dilatant cataclastic flow is associated with a significant increase in permeability; the associated yield stress has a positive dependence on pressure. In rocks with a high initial porosity, internal cracking promotes inelastic compaction; this phase is known as compactive cataclastic flow. There is an observed decrease in permeability, and the yield stress has an inverse dependence on the effective confining pressure (Zhu and Wong,

1997). In compactive cataclastic flow, a reduction in pore space is seen as a function of increasing pressure, and, consequently decreases the permeability. However, as pressure increases, the rock transitions from brittle to plastic deformation, and the rock will begin to fracture, creating microcracks. These cracks provide additional pore space. Dilatancy is a precursor to, and therefore, critical for the development of brittle faulting (Brace, 1978). Conversely, compaction promotes a reduction in porosity. Porosity change is closely related to failure mode, whereas brittle faulting is largely based on a change in pore volume. Deformation by crystal plasticity does not involve any volumetric change (Vajdova et al., 2004a; Paterson, 1978). Observations of the dominant deformation mechanism will provide insight as to whether porosity and permeability increase or decrease with increasing pressure and temperature conditions. If either collapsing pore space or non-connective cracking dominate, then permeability will decrease.

Whereas plastic pore collapse indicates ductile failure, wing cracking corresponds to brittle failure. There are material defects in every orientation; if these defects reach the optimized failure angle, they will fail. Prior to failure, the material slides; this is known as wing cracking. Wing cracks originate at the tips of the defects. They are not pure shear, meaning that there is no volumetric change.

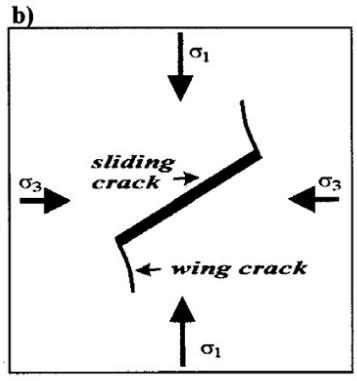

Fig. 3: Wing cracks originate at the tips of defects in a rock. Sliding of the material is observed prior to failure. (Vajdova et al., 2004a)

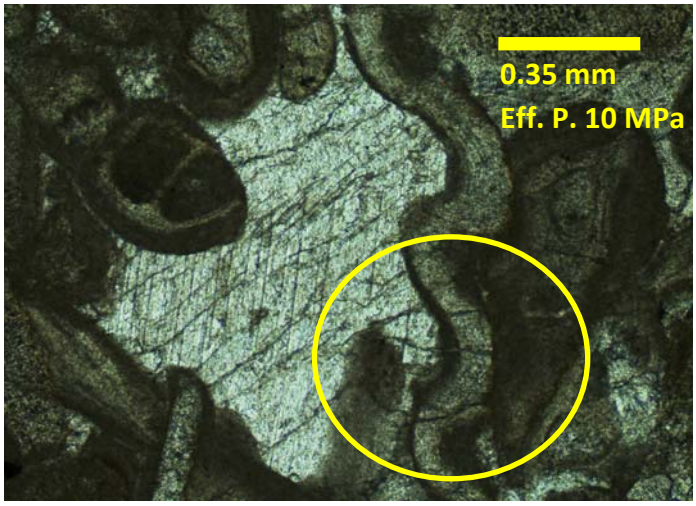

Fig. 4: Microcracks observed in deformed Indiana Limestone. Transgranular cracks, circled above, are indicative of a shear-induced increase in dislocation density (Gold, 2003).

If microcracks dominate, creating sufficiently connective pathway for the flow of fluid, the permeability will increase. If microcracks do not create connecting pathways, permeability cannot increase. It is important to note the difference between an increase in pore volume and an increase in permeability. An increase in pore volume cause by non-connective microcracks does not enhance permeability. Further, as seen from sample to sample, different temperatures and pressures will result in the observation of different deformation mechanisms.

Recently, there has been an increase in the amount of experiments observing fluid transport property evolution in limestone. Porosity in limestone ranges from 0.5% to > 20%; this variability creates complex situations for the investigation of the effects of high pressure and temperature on the deformation path. Previous experiments on the Tavel, Solnhofen and Indiana limestones showed a positive correlation between compressibility and porosity; because the bulk modulus is the reciprocal of compressibility, there is a negative correlation between porosity and the bulk modulus. Additionally, with increasing porosity, the brittle strength as well as the critical stress needed for the onset of pore collapse decreases.

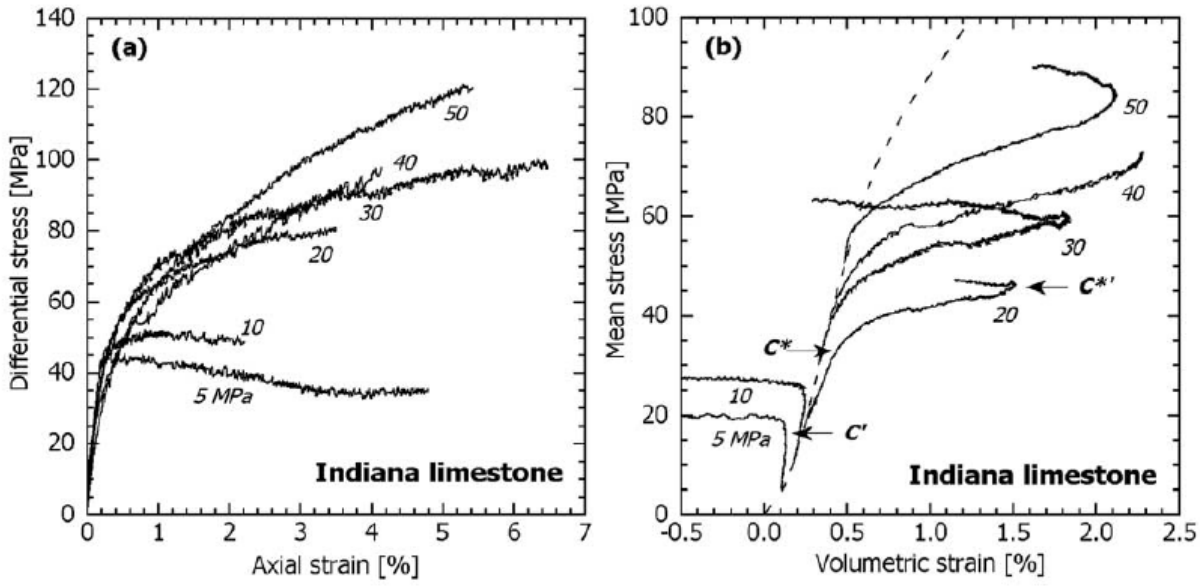

Vajdova et al., 2004a

Fig. 5: Stress-strain analyses of Indiana Limestone samples. The numbers next to each curve indicate the confining pressure maintained during each experiment. Young's modulus is represented in (a). Inflection points indicate the onset of dilatancy. Bulk modulus is given in (b), where the brittle-ductile deformation transition is tracked. The onset of pore collapse (compaction), C*, is seen right before the inflection point. Just beyond the inflection is the onset of dilatancy, C'. C*' is the transition between the two, and is marked at the peak of the inflection.

The application of a non-hydrostatic stress consequently induces a significant reduction in porosity if the applied stress exceeds a threshold (Zhu, 2006). This critical stress is referred to as shear-enhanced compaction, denoted as C*. In the shear-enhanced compaction phase, pore space in the rock collapses. Prior to C*, the decrease in porosity and permeability is controlled by the mean effective stress ($\frac{\sigma 1-\sigma 3}{2}$). At C*, the decrease is primarily controlled by the differential stress. As differential stress increases, porosity and permeability significantly decrease. This permeability reduction is caused by microcrack-induced grain crushing and by the collapse of pore space. Beyond C*, reduction in porosity and permeability reduction slows down. Stress induces pore space to either collapse or dilate, both of which affect transport properties.

Deformation itself can change the strength of a rock. As a result of strain, a rock may experience either strain hardening (Fig. 6) or strain softening (Fig. 7). A rock becomes harder and more difficult to deform during strain hardening, whereas strain softening, a result of grain crushing, ultimately results in a weaker rock. Strain softening failure behavior takes on two types: class I is stable, where the post-failure slope is consistently negative. In some cases, a rock's post-failure response can be so unstable as to invert itself. This is categorized as class II behavior. Class II rocks will fail explosively, even if the rock is infinitely stiff. The stiffness of a rock depends on the Young's modulus and its geometry. As confining pressure increases, porous rocks undergo a transition from strain softening to strain hardening. Identifying a rock as having class I or class II behavior via a stress– strain plot can help identify shear localization.

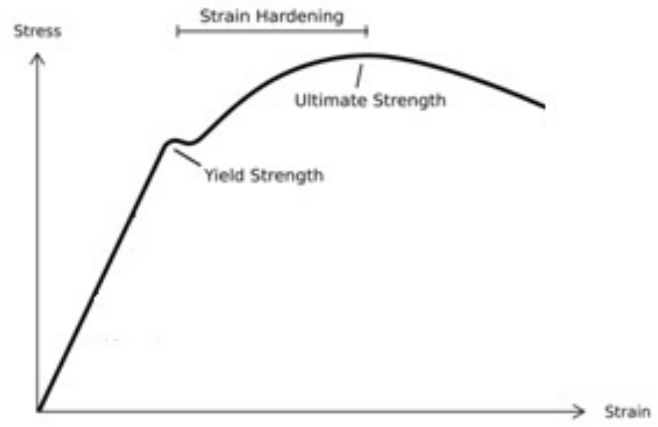

Fig. 6: Strain hardening, modified from [1]

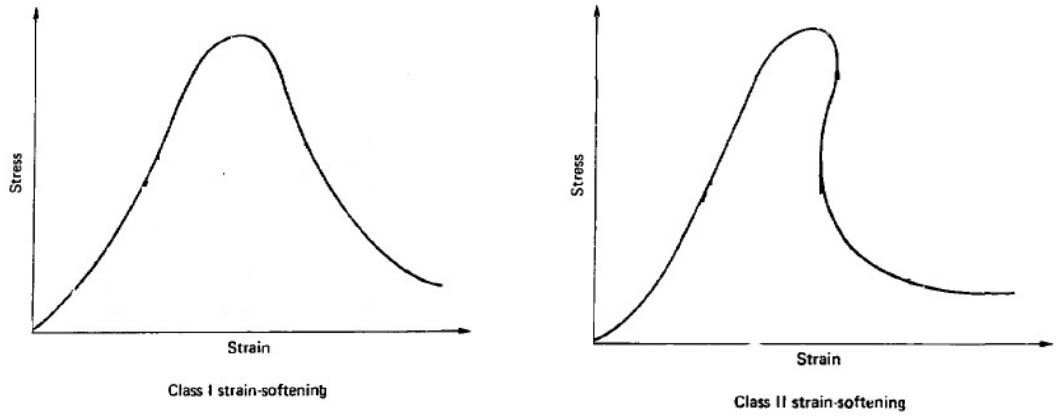

Fig. 7: Class I (left) and II (right) strain softening. Modified from Heuze et al., 1981.

Plastic deformation has not been observed in quartz-based rocks at pressures and temperatures readily attainable in the laboratory. However, calcite-based rocks have frequently been observed to deform plastically. Crystal plasticity describes the permanent deformation of crystalline material via slip and twinning within the grains (Paterson, 1978). Essentially, crystal plasticity is a manifestation of the shifting of atoms under an applied stress. Crystal plasticity, like brittle deformation, is inelastic. However, with crystal plasticity, bonds between atoms are not broken; the bonds may shift, but they still exist. Crystal plasticity can lead to brittle deformation via the areas of weakness created by dislocation slip and twinning.

1.3 Background

Indiana Limestone, also known as the Salem or Bedford Limestone, occurs in south central Indiana. Its uniform texture and grade makes it the highest quality quarried limestone in the United States. During the Middle-to-Late Mississippian Period (335-340 Ma), present-day North America was covered by shallow seas, where limestone accumulated on the seafloor. It is a calcarenite limestone, meaning that it formed from the percolation of water through calcareous shell fragments. It contains numerous fossil species including foraminifera, bryozoans, and

crinoids (Fig. G). The site of Indiana Limestone was several hundred kilometers inshore of the paleosea, but its extreme homogeneity indicates that there was enough energy to sort the sediment. However, bryozoans and crinoids lived in low energy environments; observations of mostly intact fossils indicate that they were transported, but only a small distance. Indiana Limestone is extremely homogeneous, being composed of ~97% calcite ($CaCO_3$) and ~3% magnesite ($MgCO_3$); its chemical composition makes for an excellent specimen in which to observe calcite deformation

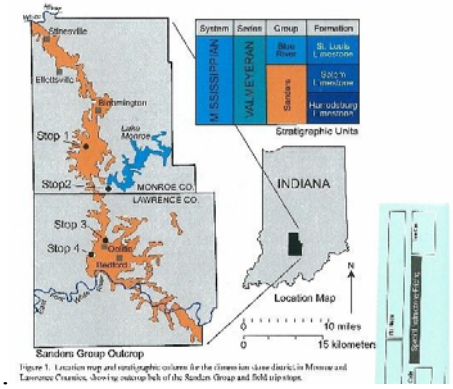

Fig 8: Location of Indiana Limestone[++]

2. Objectives of Research

Analyses of Indiana Limestone cores subjected to deformation experiments allow us to determine how porosity and permeability are affected with increasing temperature and pressure. Examination of change in pore volume and microcrack creation in these samples establish which factor dominates as temperature and pressure increase. Rock deformation behavior has applications in the construction, groundwater, and energy exploration industries; on a larger scale, it also applies to understanding earthquake mechanics and how they affect surrounding areas.

2.1 Hypotheses

My first hypothesis is that crystal plasticity will play an important role in the deformation behavior of Indiana Limestone. Crystal plasticity, as with brittle fracture, is an inelastic deformation behavior. However, unlike brittle fracture, with crystal plasticity, the bonds between atoms are not broken. Crystal plasticity will either be seen as mechanical twinning or dislocation slip in a thin section of a post-deformation sample. The type of observed crystal plasticity is dependent on temperature; dislocation slip is unique in the fact that is it thermally activated. If the observed plastic failure in the limestone samples arises from dislocation slip, it can be inferred that the yield stress is dependent on temperature. It is important to test cores at several temperature and pressure intervals to observe what the critical temperatures and pressures are. Crystal plasticity can be a precursor to brittle fracture and will either facilitate microcracking or promote pore collapse. Creation of planes of weakness will eventually lead to failure, either seen as compaction of pore space or dilatancy due to microcracking. I further hypothesize that as temperature increases, crystal plasticity will be more pronounced. It has been observed that at higher temperatures, quartz-based granites and sandstones increasingly behave as a plastic. I subsequently hypothesize that limestone will conform to deform plastically. If evidence of

crystal plasticity such as twinning is observed, the hypotheses pass. If there is no evidence of this type of deformation, i.e. only brittle fracture is seen, the hypotheses do not pass.

3.1 Experiment Design

Cores of Indiana limestone were sent to the Rock Physics Laboratory at the University of Maryland. Measurements of weight, length, and diameter of each sample are taken with a caliper three times and then averaged. Initial porosity and permeability measurements are taken with the porosimeter and permeameter (Figs. B-E). The cores are locked into place in a steel chamber which is then pressurized at several intervals: 200 MPa, 300 MPa, and 400 MPa. At each interval, gas is sent upstream to obtain either porosity or permeability measurements at each pressure. Nitrogen gas is used for confining pressure and helium gas is used as the penetrative substance. The helium molecules are small enough to be able to penetrate into miniscule pore spaces. This method allows for higher precision than water saturation because helium molecules are smaller than water molecules. The porosimeter measures the volume of gas used to obtain porosity and the permeameter determines flow rate to obtain permeability. The porosity and permeability data are indicative of whether the rock cores are of relatively uniform composition or are anomalously heterogeneous. Variation in porosity or permeability between samples indicates heterogeneity in rock composition and/or grain size.

The cores are then oven-dried for at least 48 hours at 40 degrees Celsius to achieve a nominal dry status. Porosity, permeability and weight measurements are re-taken to achieve the nominal dry measurement. The sample is then saturated overnight with distilled water in a vacuum chamber. It is then jacketed with a 0.005” thick copper foil, which is soldered securely around the sample.

The plain-jacketed sample is then loaded into the Autolab 1500c where it is exposed to hydrostatic conditions of confining pressure 10 MPa but no pore pressure. The purpose of exposing the core to a low pressure prior to attaching the strain gages is to more securely adhere the copper jacket to the sample and to minimize damage to the strain gages after they are attached. When exposed to confining pressure, the copper jacket will form to fit the outer pores of the core. If this is not done prior to attaching the strain gages, there is a risk of pitting and damaging the gages, which would lead to inaccurate readings and premature failure of the gages. After being exposed to the initial low pressure, horizontal and vertical strain gages are adhered to the sample with super glue and are subsequently soldered to strain gage leads (Fig. 9). These leads transmit the axial and radial strain signals while the experiment is performed.

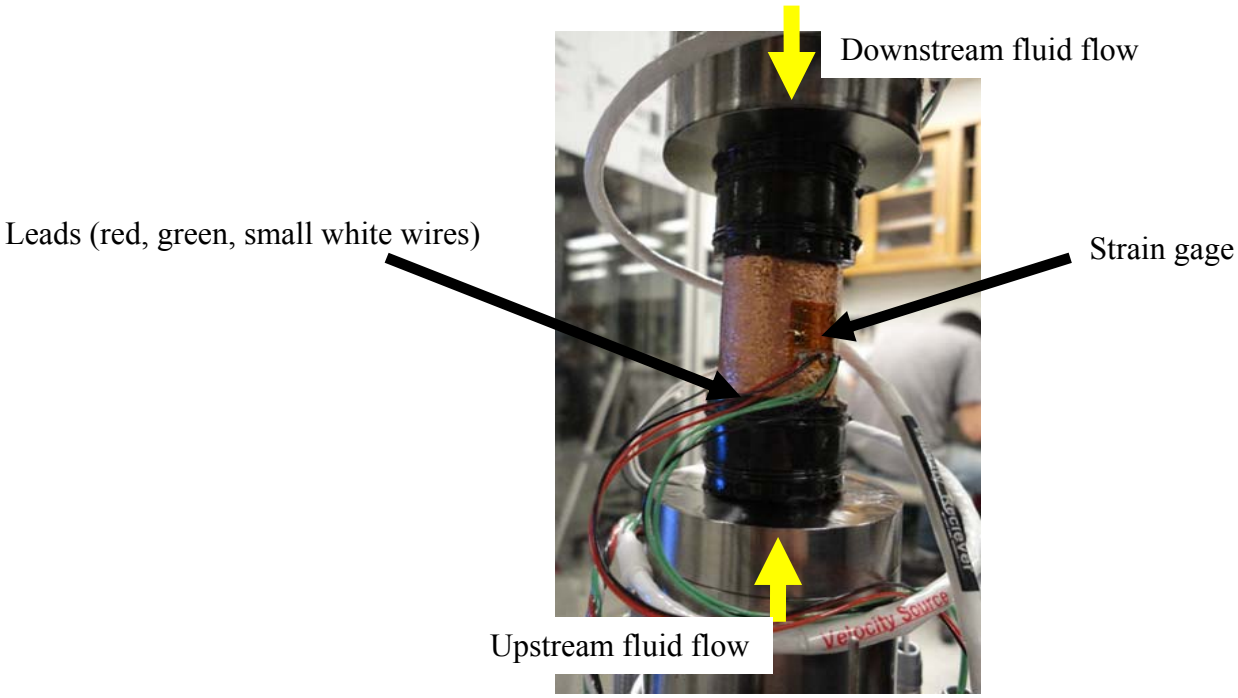

Fig. 9: Jacketed sample with attached strain gages. Yellow arrows indicated fluid flow direction through the sample.

After the completed core is loaded into the machine, confining pressure is set to 3 MPa; when this condition is met, pore pressure may be added. Confining and pore pressures are added in steps of 1 MPa until confining pressure 13 MPa and pore pressure 10 MPa conditions are reached. Each experiment has a different set of pressure and temperature upper constraints (Fig. 10, below). If it is a high-temperature experiment, the furnace will need to be set to the desired temperature before continuing to higher pressures. During triaxial experiments, the strain rate maintained throughout the experiment is $10^{-5}s^{-1}$. Observations of deformation are noted by monitoring strain gage behavior and differential stress readouts. When the deformation portion of the experiment is completed, the sample must be slowly unloaded. If a sample is unloaded too quickly, additional damage could be incurred, which would not reflect accurately upon the triaxial experiment. Post-experiment microscopic analysis of thin sections obtains qualitative and quantitative information about the deformation, including the abundance of twinning and microcracking (Figs. 18 & 19). Macroscopically, elastic modulii and inelastic property evolution are calculated. Elastic modulii are the physical properties of a material which characterize mechanical response. For each experiment, I have calculated elastic modulii including bulk modulus and Young's modulus as well as inelastic property evolution such as changes in permeability and porosity.

Core	Effective Pressure	Pressure Conditions	Temperature
3-1a	50	Triaxial	25
3-1b	10	Triaxial	25
3-2a	70	Hydrostatic	25
3-2b	70	Hydrostatic	50
3-3a	126	Hydrostatic	25
3-3b	50	Hydrostatic	136
3-4b	126	Hydrostatic	25
3-11a	10	Triaxial	50
3-16a	123	Hydrostatic	50

Fig. 10: Completed experiments and their respective conditions.

Error analysis is imperative for a well-rounded and scientifically complete experiment. Standard deviation, a measurement of variability; shows how much dispersion there is from the average of collected data. The standard deviation, σ, is expressed as $\sigma=\sqrt{\Sigma(x_{avg}-x_i)^2/(n-1)}$, where x_{avg} represents the average of the data points, x_i represents the initial data point, and n the number of data points. Variability within undeformed samples is calculated for porosity and permeability (Fig. 12). All data fall within a 2σ range of the mean.

3.2 Calibrations & Uncertainties

Several calibration techniques are used to standardize our data:

Head-to-head load cell calibration is used to for setting a reference point for P and S wave arrival time. The purpose of high-temperature head-to-head calibration is to determine how changes in temperature affect signal arrival time between the two steel velocity heads; no sample is involved. Two steel velocity heads are jacketed together (Fig. 11) with a thin layer of shear gel between them. This shear gel will pick up and transmit the signal from the source to the receiver. This setup is loaded and confining pressure is applied; at room temperature, a signal is sent and recorded. This is repeated every 10°C until the maximum high temperature is reached at 150° C. After all signals have been recorded, first arrival times of P-waves are determined for each measurement. These times are put into the velocity calibration file which will then be used as the reference settings for future high-temperature experiments.

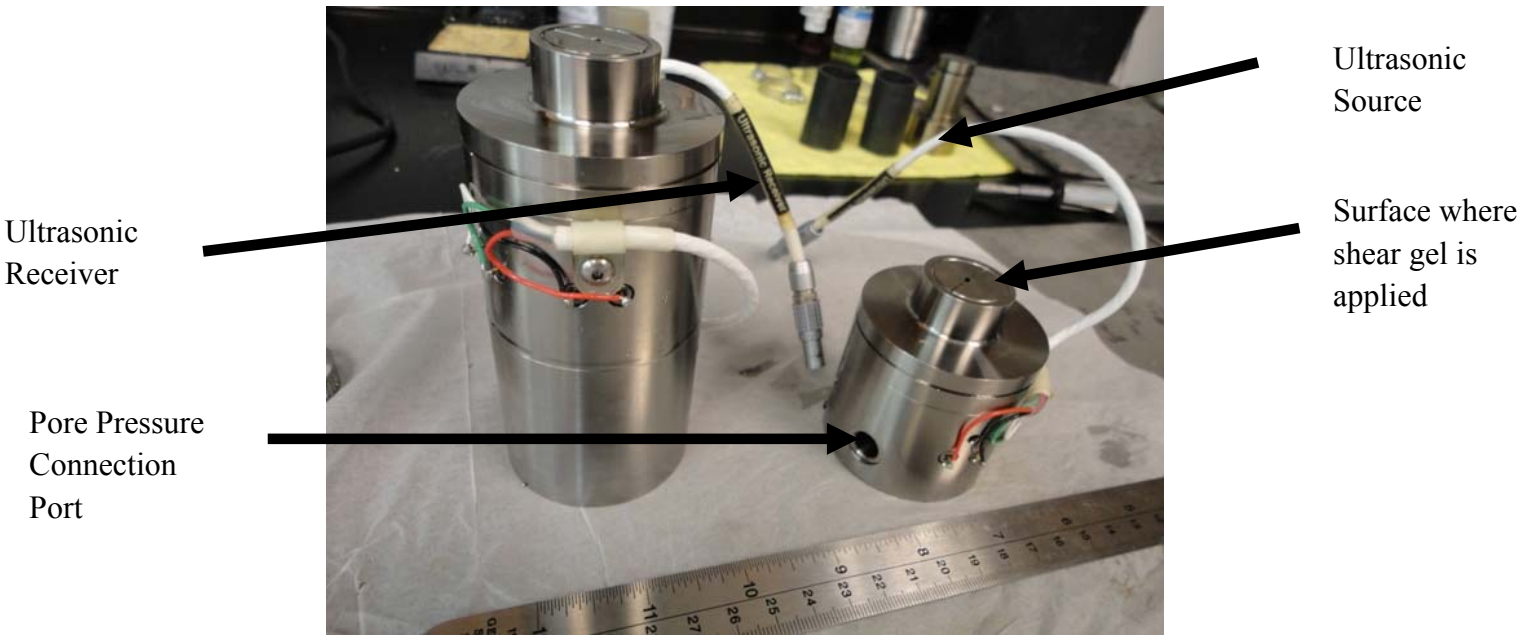

Fig. 11: Setup of head-to-head calibration experiment. Two steel heads are sandwiched together; no core is used. The resulting waveform data sets the reference point for when cores are used.

To ensure that the deformation heads and load cell are properly calibrated, experiments are conducted on a core with known elastic modulii, such as aluminum. The aluminum core is tested at the desired conditions; the bulk and Young's modulus are then calculated from the data and compared to known values. Similarly, cores with known permeability are used for permeameter calibration.

To calibrate the porosimeter, differently-sized and weighted steel cores are stacked on top of each other in a chamber. The steel cores can be stacked in any order, as long as at least one core is left out (Figs. B-E). The volume of the left-out core is calculated as a "pore volume" calculation. The measurements are taken four more times with different arrangements of the cores. This standardizes the pore volume reference point and calibrates the porosimeter for core testing.

3.3 Strain Gage Uncertainties

Strain gages convert changes in a sample's dimensions into an electronic signal that is received and interpreted as deformation. The strain gage experiences mechanical deformation when there is an applied force; this deformation results in a small change in gage resistance, which is proportional to the magnitude of the applied force. This applied force changes the cross-sectional area of the gage, subsequently changing the gage factor.

Vertical strain gage 1: Gage Factor @ 24°C = 2.090 $\pm$ 0.5%

Vertical strain gage 2: Gage Factor @ 24°C = 2.085 $\pm$ 0.5%

Horizontal strain gage: Gage Factor @ 24°C = 2.050 $\pm$ 0.5%

Each gage has an uncertainty of 0.5%. Three gages are used per sample; assuming maximum error per gage, the uncertainty due to the strain gages is 1.5% per measurement. This applies to

the volumetric strain, which is used for calculating bulk modulus, axial strain, used for Young's modulus, as well as other deformation properties. Strain gage material expands with increasing temperature; there is an additional temperature coefficient for calculating high-temperature strain error.

4. Results

Initial porosity and permeability measurements of all cores are taken. The data are then subsequently plotted as permeability versus porosity to observe for uniformity among the sample. The average porosity is 16.3% and the average permeability is 1.2 mD. There is an observed general positive trend between porosity and permeability.

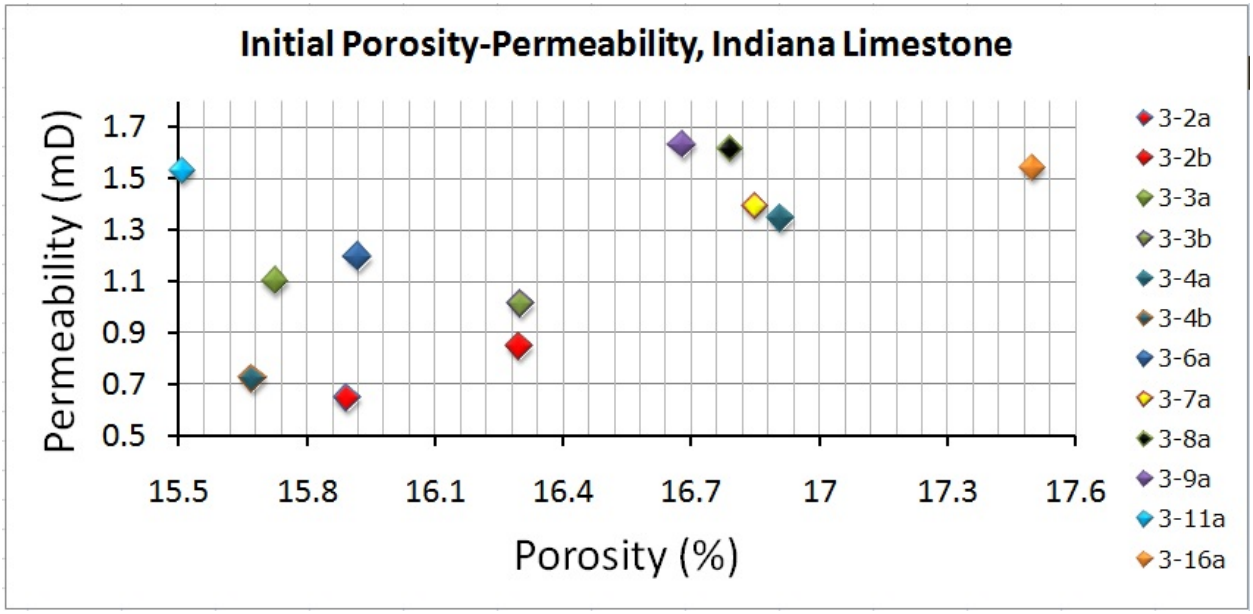

Fig. 12: Porosity-Permeability. The average porosity is 16.3% and the average permeability is 1.2 mD.

Bulk modulus (K) is a measure of a material's resistance to compression. It shows what pressure increase is needed to obtain a relative decrease in volume. Effective pressure (MPa) is plotted versus volumetric strain (%) to obtain the bulk modulus. It is mathematically expressed as:

$$K = -V\left(\frac{\partial p}{\partial V}\right)$$

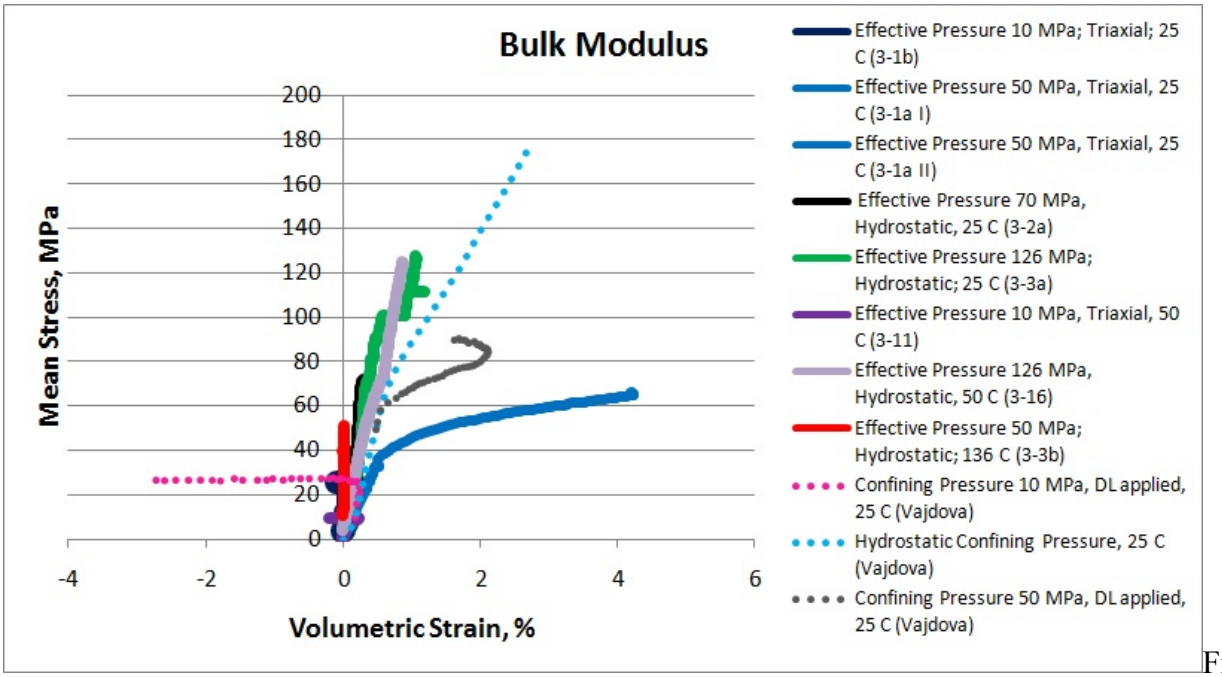

Fig. 13: Bulk modulus. There is an observed positive trend between temperature and stiffness of the bulk modulus (25°, 50°, 136° C; core 3-1a, 3-16, and 3-3b, respectively).

Young's modulus (E) is the measure of the stiffness of a material. Young's modulus shows how much a material either stretches under tension or shrinks under compression; it is only obtained during triaxial experiments by plotting the differential stress (MPa) versus axial strain (%). Young's modulus is the ratio of differential stress to axial strain:

$$\mathbf{E} = \frac{\sigma\ differential}{\varepsilon\ axial}$$

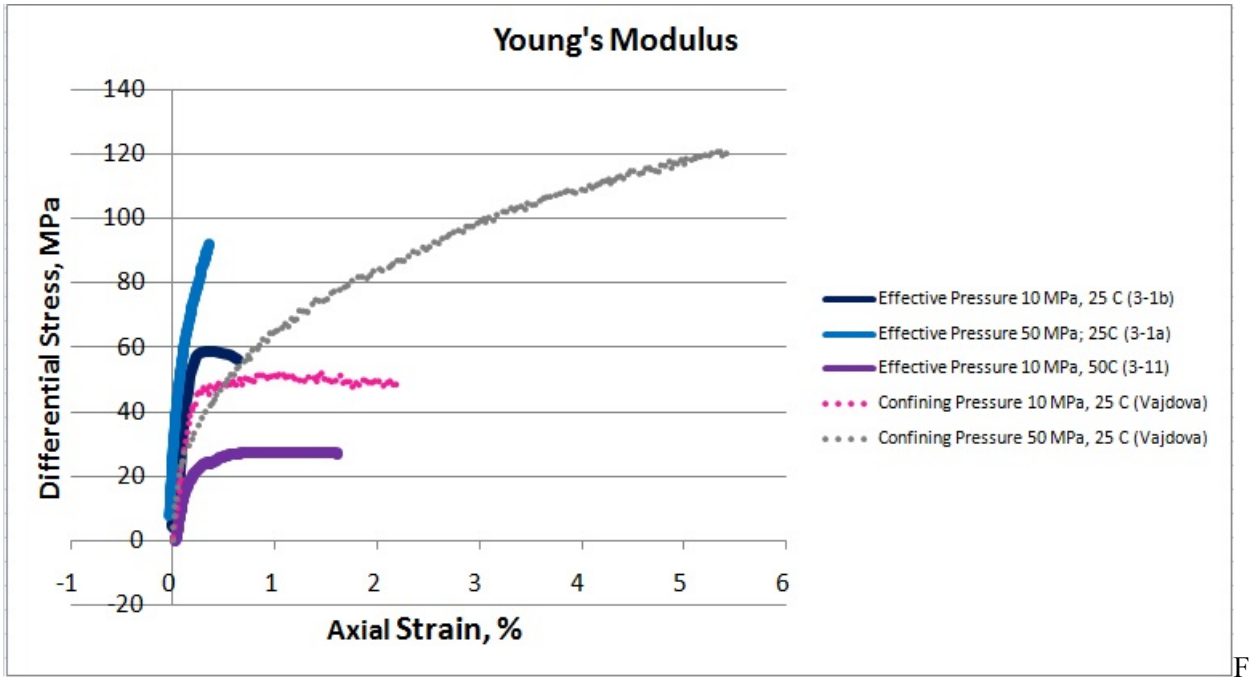

Fig. 14: Young's modulus. Core 3-11, at 50° C, has a lower onset of dilatancy than both room temperature experiments at the same effective pressure and those at higher effective pressure.

Permeability measurements are taken as effective pressure/stress is increased. They are subsequently plotted to monitor for significant change and are further separated into hydrostatic and triaxial. There are two predominant methods in which to measure permeability, A-spike and Steady-state. A-spike involves varying the downstream pore pressure while keeping upstream pore pressure constant (Fig. 9). This creates a temporary "spike" in fluid flow, from which the permeability can be calculated. With the Steady-state method, fluid flow rate is measured at intervals where the upstream pore pressure increases and remains steady for the period of the measurement; downstream pore pressure is kept constant. This creates the steady flow rate conditions for which the method is named. Permeability is calculated by fitting the sample response to analytical solutions. These methods are suitable for rocks with initial permeability between 5 mD and 0.5 D, well within the range seen in Indiana Limestone.

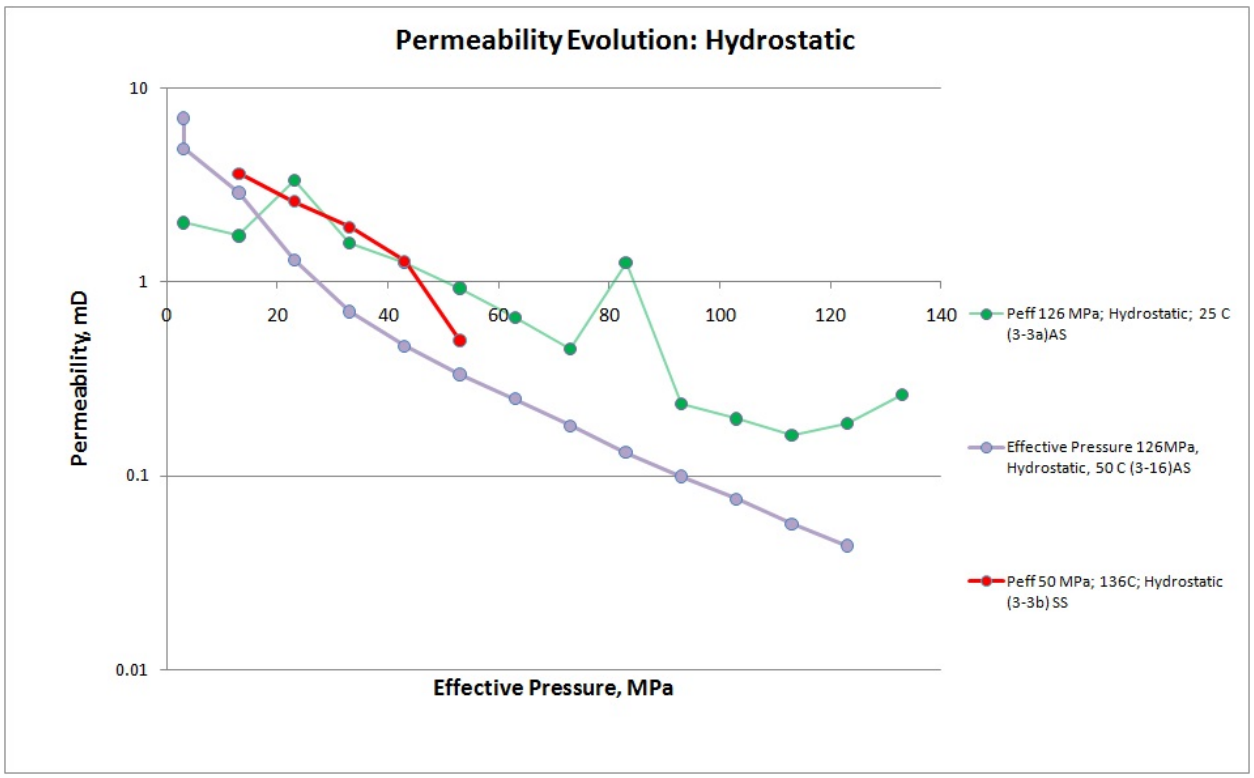

Fig. 15: Permeability evolution in hydrostatic pressure experiments at room temperature (25° C) and two elevated temperatures (50°C and 136°C).

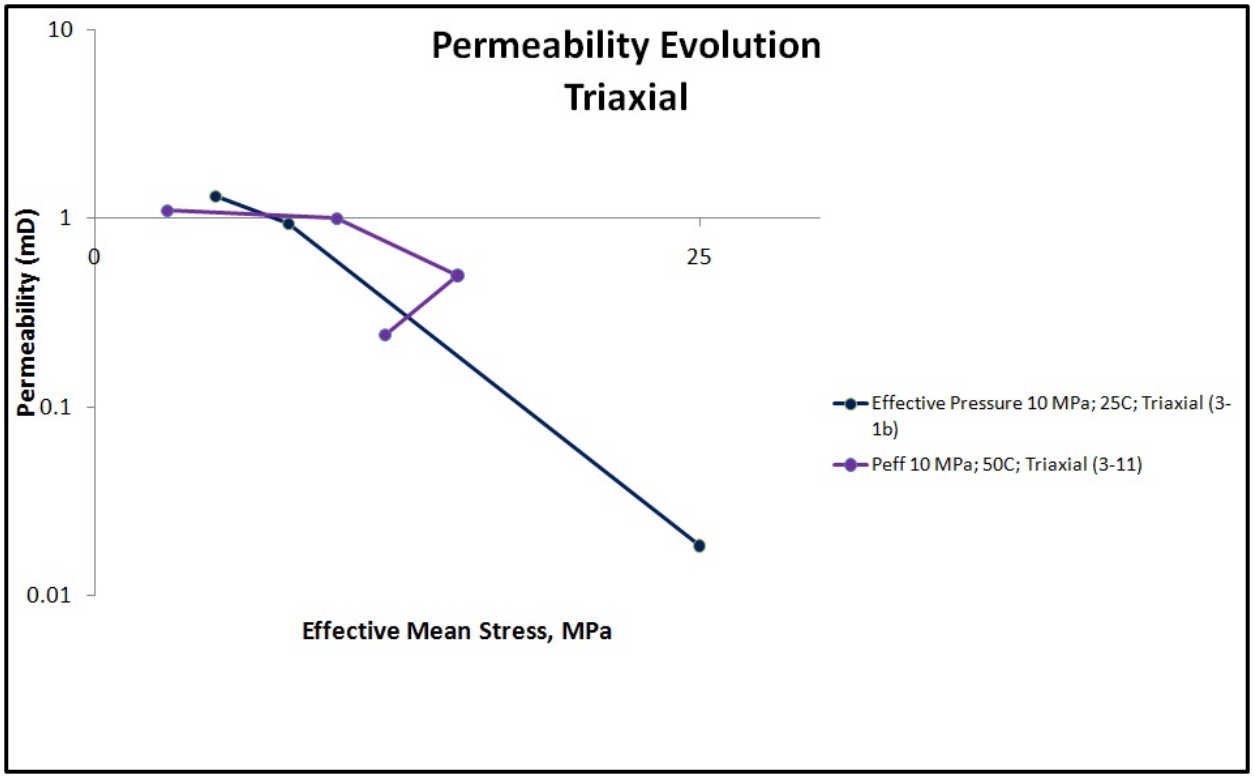

Fig.16: Permeability evolution as effective stress increases, triaxial experiments at 25°C & 50°C.

Velocity measurements allow for monitoring of sample density. Initially, as pressure or stress increases, the limestone becomes compacted and the wave is able to travel faster. Relatively large increases or decreases in sample velocity are indicative of the onset of pore space compaction and dilatancy.

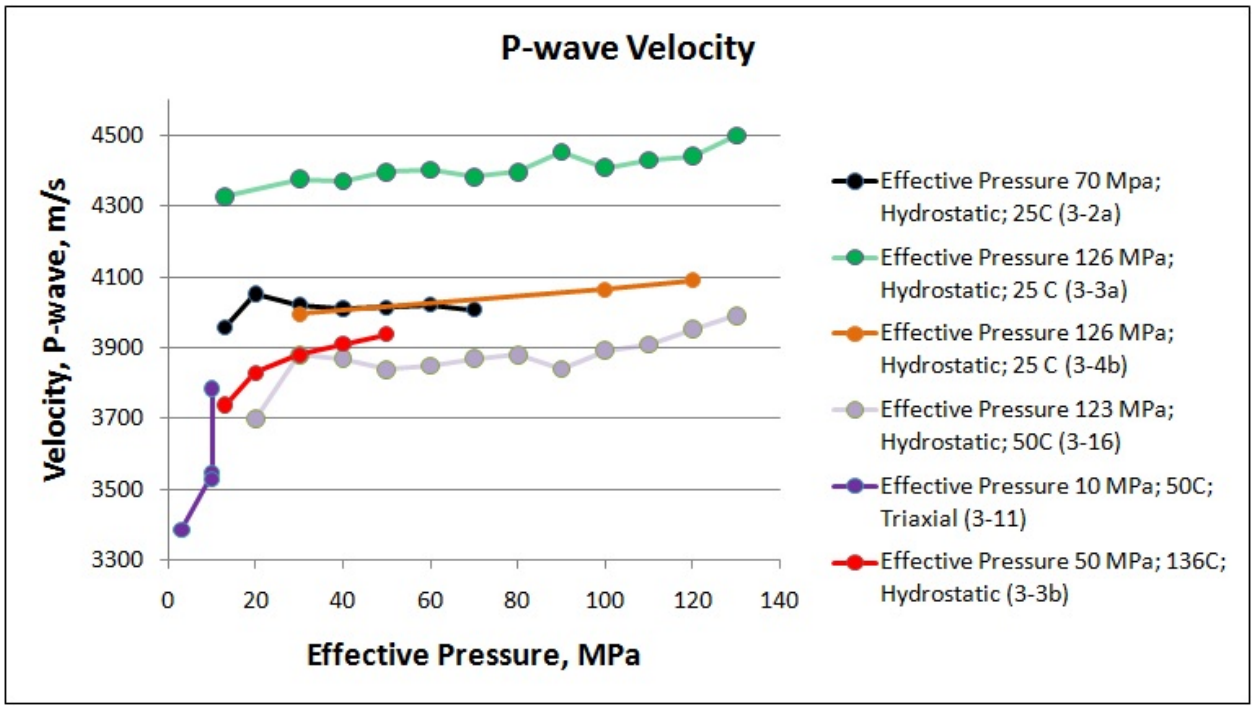

Fig. 17: Velocity measurements as a function of increasing effective pressure.

Quantitative measurements of twin and microcrack occurrences are documented for two triaxial cores and one undeformed core. Each core is divided into sections of equal area (Appendix D, Figure 1). The occurrences are then converted to a twin-and-microcrack density per square inch and are plotted for comparison.

Core	Twin Count	Microcrack Count
3-4a (undeformed)		
> Section 1	5	3
> Section 2	2	3
> Section 3	1	3
> Section 4	1	2
Average Count	2	3
3-1a (Effective P 50 MPa)		
> Section 1	3	4

> Section 2	4	15
> Section 3	7	10
> Section 4	2	13
> Section 5	3	5
> Section 6	3	10
> Section 7	4	10
> Section 8	1	20
Average Count	3	11
3-1b (Effective P 10 MPa)		
> Section 1	3	12
> Section 2	1	7
> Section 3	3	13
> Section 4	3	11
> Section 5	1	6
> Section 6	4	15
> Section 7	0	8
> Section 8	3	7
Average Count	2	10

Fig. 18

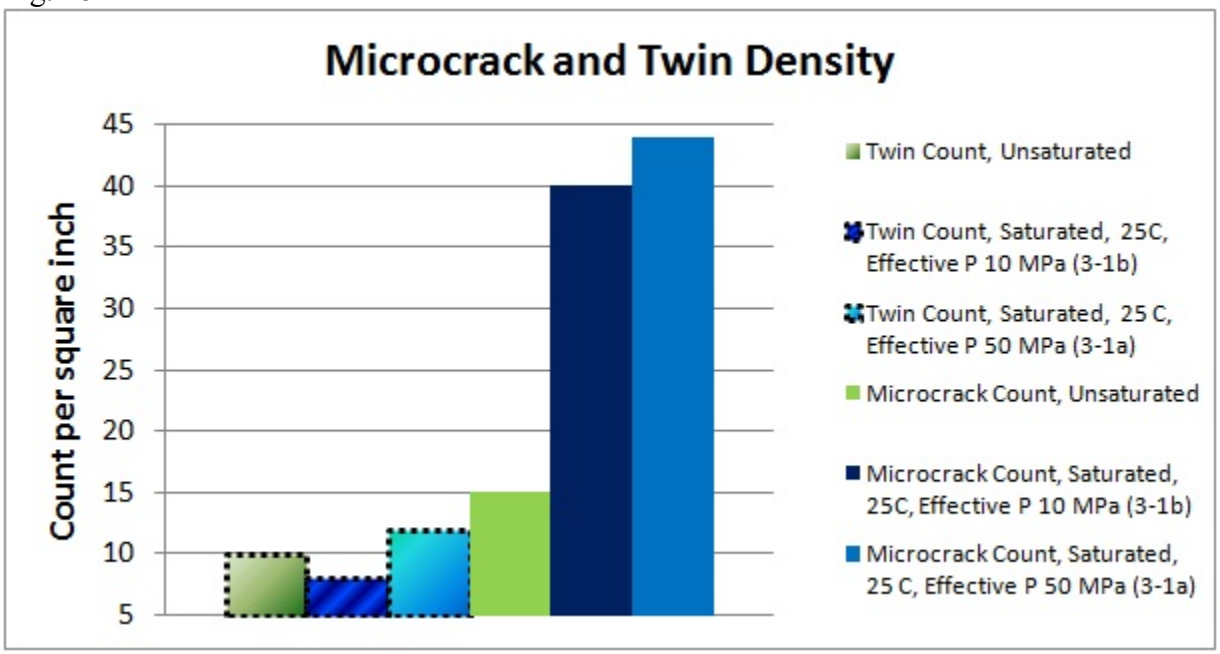

Fig. 19: Microcrack and twin density count.

5. Discussion of Results

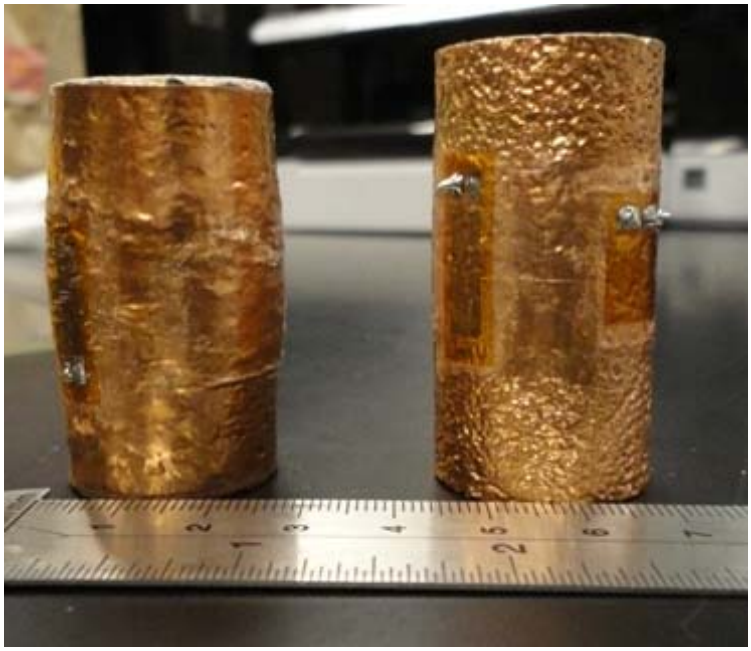

Fig. 20: Left: Core 3-11, right: core 3-16. Core 3-11 was deformed triaxially at 50°C and clearly exhibits characteristics of plastic deformation (bulging core with no macroscopic fracture). Core 3-16 was deformed hydrostatically at 50°C and shows no macroscopic indication of plastic deformation. Further confirmation will be done with quantitative thin section analysis, where evidence of crystal plasticity can be detected from twin counts.

Bulk Modulus

There is a positive correlation between experiment temperature and stiffness of the bulk modulus. This is specific between the 25°C (3-1a), 50°C (3-16), and 136°C (3-3b) cores. Additionally, the effect of water weakening on sample is apparent via comparison to the Vajdova et al. data. Those previous experiments were conducted on dry samples; our experiments involved saturated cores with pore fluid maintained throughout the experiment.

Specific examples include the comparison between Vajdova experiment at 50 MPa and UMD core 3-1a, also a triaxial experiment at an effective pressure of 50 MPa. The UMD core experiences a much higher amount of volumetric strain relative to the Vajdova core at a much lower mean stress. It is possible that water saturation promotes pore collapse at an earlier stage of deformation, but would likely have minimal effect on crystal plasticity. This is because crystal plasticity occurs as a function of the degree of deformation and is independent of the effective pressure maintained throughout the experiment.

Core 3-1b, held at room temperature with an effective pressure of 10 MPa, follows the similar Vajdova core. The degree of negative volumetric strain (tension) experienced is much less than that of the previous experiment. However, this is reasonable because if water saturation weakens a sample, that sample should experience less tension and more compression (positive

volumetric strain). These data are consistent with my hypothesis that crystal plasticity affects bulk deformation behavior and will be more pronounced at higher temperatures.

Young's Modulus

The effect of temperature on onset of dilatancy is dramatic. UMD core 3-11 (50° C) has a drastically lower inflection point compared to both the UMD 25°C experiments and the Vajdova et al. dry cores at 25°C. The onset of dilatancy occurs at a differential stress of ~25 MPa compared to ~60 MPa (UMD) and ~45 MPa (Vajdova et al.).

Permeability Evolution

Hydrostatic: Overall decrease in permeability throughout all samples. With increasing temperature, decrease is slightly more rapid.

Triaxial: Two cores were plotted: room temperature (3-1b) and elevated temperature (3-11). Both experiments were conducted at an effective pressure of 10 MPa; there was about an order of magnitude greater decrease in permeability in the room temperature core. This is reasonable and consistent with my hypotheses because all other variables equal, at elevated temperatures, a rock is more prone to dilation at lower pressure/stress. Given that limestone has a positive porosity-permeability relationship, as dilatancy occurs, a reduction in permeability decrease is to be expected.

Velocity Measurements

Among the room temperature experiments (3-2a, 3-3a, 3-4b), there is an observed overall increase in velocity in all samples. This is reasonable because initially, the rock becomes more compact due to increasing pressure. This allows for the wave to travel through the core faster. There is a noticeable trend that higher pressures cause velocity to increase even further.

There is an even more noticeable change in velocity among the elevated temperature cores. The hydrostatic core has a larger increase in velocity compared to room temperature cores; the triaxial experiment has a drastic increase in P-wave velocity. This makes sense because at first, the rock compacts, increasing velocity. If dilatancy occurs, that would counteract the effect from the initial compaction; velocity would then decrease.

Conclusions

Transport properties such as porosity and permeability affect fluid flow. When subject to an applied stress or change in pore pressure, a rock will respond with either a compaction or dilation of pore space, consequently affecting these transport properties. The capability to understand and predict the occurrence and degree of deformation is based on a fundamental understanding of the failure mode, inelastic behavior, and brittle-ductile transition. Rock deformation applies to the construction, groundwater, and energy industries as well as determining how earthquakes affect the immediate and surrounding areas. Transport property evolution was monitored during deformation experiments on Indiana Limestone. The data shows a positive trend between increasing temperature and magnitude of deformation such as change in pore volume and the elastic modulii. In core 3-11, a triaxial experiment conducted at 50°C, there is a direct indication that crystal plasticity has occurred; the core is permanently bulging,

indicating a high degree of deformation. However, it does not have a macroscopic plane of failure. This observation is quite consistent with my hypotheses that crystal plasticity has a major role in the deformation. Other methods for detecting crystal plasticity include point counts in thin section of deformed samples; of the ones observed, those experiments held at higher effective pressures experienced a much higher degree of crystal plasticity (twinning). Together, these data support my hypotheses that crystal plasticity affects the bulk deformation behavior in limestone and that with increasing temperature, crystal plasticity is more pronounced. We were also able to show a weakening effect that water saturation has on the elastic modulii by comparing our results to those of previous experiments by Vajdova et al. Our data indicates that water saturation initiates a weakening effect in the cores. In order to further explain this phenomenon, additional experiments need to be conducted at elevated temperatures and variable pressure/stress conditions. Completed experiments need to be repeated in order to ensure that data is not inaccurate.

Acknowledgements

I would first like to thank my advisor, Dr. Wen-lu Zhu for her generous support and for giving me the opportunity to learn the necessary skills required for this research experiment. I would also like to thank graduate students Tommy Tamarkin and Jill Gribbin as well as Harry Lisabeth for their help in training me on the porosimeter, permeameter, triaxial deformation machine, and helping me with sample preparation. The staff of New England Research, producers of the Autolab 1500c, welcomed us into their workplace for a week while we got acquainted with and trained on how to operate the machine. Lastly, this project would not exist without funding from ExxonMobil.

References

Baud, P., Schubnel, A., and Wong, T.f. (2000), Dilatancy, compaction, and failure mode in Solnhofen limestone. *J. Geophys. Res.*,Vol. 105, No. B8, pp. 19,289-19,303, 2000 doi: 10.1029/2000JB900133

Brace, W. F., and E. G. Bombolakis (1963), A Note on Brittle Crack Growth in Compression, *J. Geophys. Res.*, 68(12), 3709–3713, doi:10.1029/JZ068i012p03709

Brace, W.F., Walsh, J.B., Frangos, W.T., Permeability of Granite Under High Pressure, 1968, J. Geophys. Res., Vol. 73 No. 6

Brown, Mark A., Archer, Allen W., Kvale, Erik P. (1990), Neap-Spring Tidal Cyclicity in Laminated Carbonate Channel-Fill Deposits and its Implications: Salem Limestone (Mississippian), Indiana, USA. Journal of Sedimentary Petrology, Vol. 60, No. 1, January, 1990, pages 152-159

Evans, Brian and Wong, Teng-fong (1992), Fault Mechanics and Transport Properties of Rocks: A Festschrift in Honor of W.F. Brace. Academic Press, Inc.

Freeze, R.A. and Cherry, J.A. 1979; *Groundwater*. Hemel Hempstead: Prentice Hall International. xviii + 604 pp.

Frew, D J, Akers, S A, Chen, W, and Green, Mark L. (2010), Development of a dynamic triaxial Kolsky bar, *Meas. Sci. Technol.* 21 (2010) 105704 (10pp) doi:10.1088/0957-0233/21/10/105704

H. GERCEK; "*Poisson's ratio values for rocks*"; International Journal of Rock Mechanics and Mining Sciences; Elsevier; January 2007; 44 (1): pp. 1–13.

L.W. Gold.1 Researcher Emeritus, Institute for Marine Dynamics, National Research Council of Canada, Kerwin Place and Arctic Ave., Memorial University, P.O. Box 12093, Station A, St. John's, NL A1B 3T5, Canada.

Hadley, Kate. Comparison of Calculated and Observed Crack Densities and Seismic Velocities in Westerly Granite, 1976, J. Geophys. Res., Vol. 81, No. 20
Hart, D., and H. Wang (1995), Laboratory measurements of a complete set of poroelastic moduli for Berea sandstone and Indiana limestone, J. Geophys. Res., 100(B9), 17741-17751.

Heuze, Francois E., Butkovich, Theodore R., Peterson, John C., An Analysis of the "Mine-By" Experiment, Climax Granite, Nevada Test Site. Lawrence Livermore National Laboratory, Livermore, CA, DCID-19047 (1981).

[+]Indiana Geological Survey, unpublished manual. Image taken from http://dcfossils.org/index.php/gallery6/.

Paterson, Mervyn S (1978) *Experimental Rock Deformation: The Brittle Field.* Springer-Verlag, New York Heidelberg Berlin. ISBN 0-387-08835-0

Popp, Michael. Internet blog: Louisville Fossils and Beyond: Fossils in Indiana Limestone. http://louisvillefossils.blogspot.com/2010/01/fossils-in-indiana-limestone.html

Powell, Wayne G. (2004). Indiana Limestone. http://academic.brooklyn.cuny.edu/geology/powell/613webpage/NYCbuilding/IndianaLimestone/IndianaLimestone.htm

Reinhart, W.D., Vogler, T.J., Chhabildas, L.C., 2007. Strength Measurements on Dry Indiana Limestone Using Ramp Loading Techniques. *Shock Compression of Condensed Matter*, American Institute of Physics 978-7354-0469

*Vajdova, Veronika, Baud, Patrick, Wong, T.-f. (2004), *Compaction, dilatancy, and failure in porous carbonate rocks*, J.Geophys. Res., 109, B05204, doi: 10.1029/2003JB002508.

**Vajdova, Veronika, Baud, Patrick, Wong, T.-f. (2004), Permeability evolution during localized deformation in Bentheim sandstone, J. Geophys. Res., 109, B10406, doi:10.1029/2003JB002942

Vajdova, Veronika, Baud, Patrick, Wong, T.-f (2010), Micromechanics of inelastic compaction in micritic and allochemical limestones. Geophysical Research Abstracts, Vol. 12, EGU2010-2244

Wong, Teng-fong (1982), Shear Fracture Energy of Westerly Granite from Post-Failure Behavior, J. Geophys. Res., 87, 1B1502

Wong, Teng-fong and Zhu, Wenlu (1999). Brittle Faulting and Permeability Evolution: Hydromechanical Microstructural Observation, and Network Modeling. *Faults and Subsurface Fluid Flow in the Shallow Crust,* Geophysical Monograph 113

Xiao, X., *Zhu, W. and Evans, B. (2003) Deformation mechanisms and failure modes in Solnhofen limestone, *Proceedings of the 39th U.S. Rock Mechanics Symposium*, P.J. Culligan, H.H. Einstein and A.J. Whittle (editors), Soil and Rock America 2003, *1,* 453-458.

Zhu, W., P. Baud, and T. Wong (2010), Micromechanics of cataclastic pore collapse in limestone, J.Geophys. Res., 115, B04404, doi: 10.1029/2009JB006610

Zhu, Wenlu (2006), Quantitative Characterization of Permeability Reduction Associated with Compactive Cataclastic Flow. Earthquakes: Radiated Energy and the Physics of Faulting; Geophysical Monograph Series 170; doi: 10.1029/170GM15

Zhu, Wenlu and Wong, Teng-fong (1997) The transition from brittle faulting to cataclastic flow in porous sandstones: permeability evolution, *Journal of Geophysical Research*, *102*, 3027-3041

* 2004a

** 2004b

Zoback, M.D. and Byerlee, J.D. (1975), Permeability and Effective Stress. *AAPG Bulletin*; January 1975; v. 59; no. 1; p. 154-158

1.http://upload.wikimedia.org/wikipedia/commons/thumb/8/84/Stress_Strain_Ductile_Material.png/800px-Stress_Strain_Ductile_Material.png

Appendix A: Figures

Fig. A: Deformation machine, Autolab 1500c.

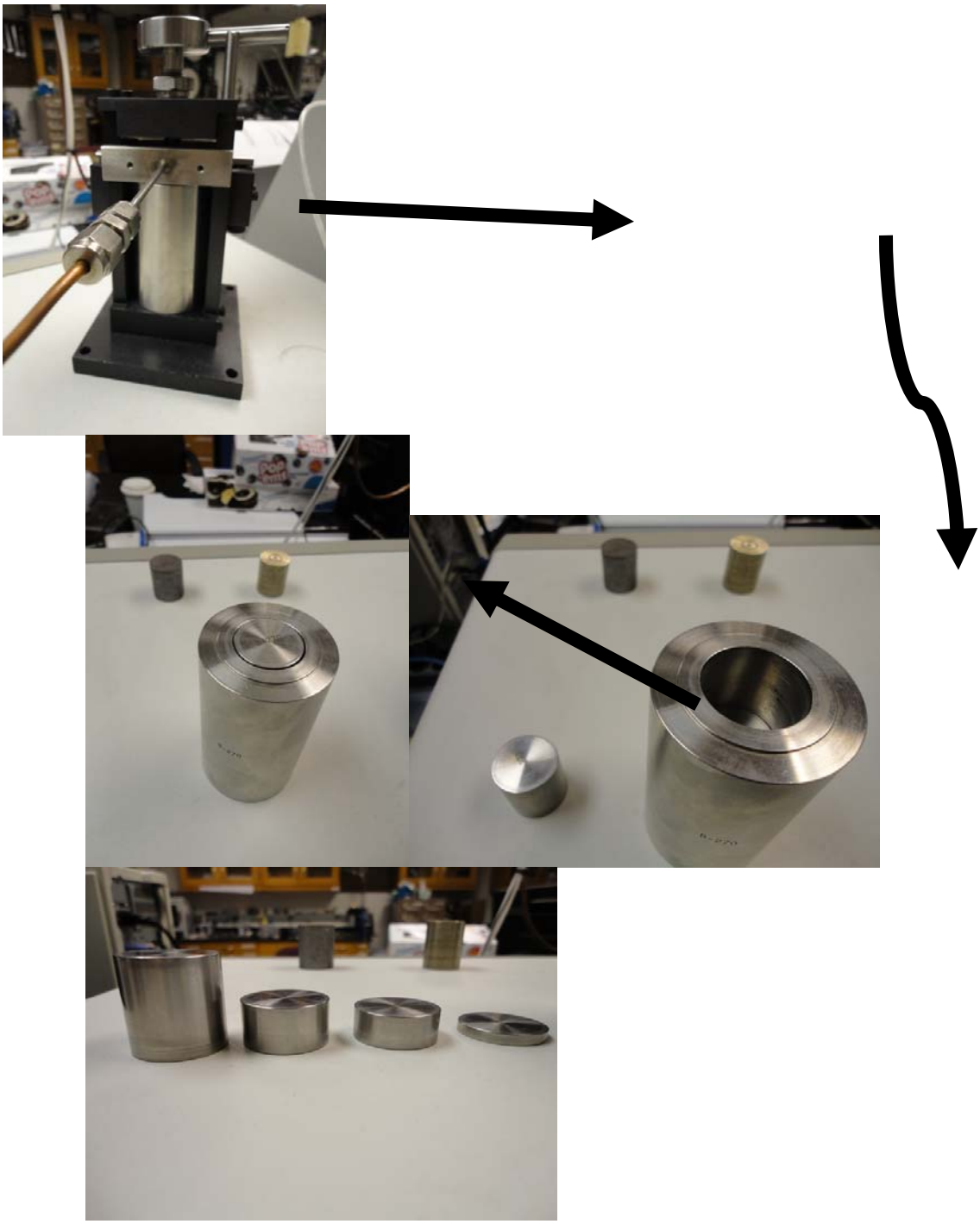

Clockwise, Figs. B-E: Porosimeter attachment. Upper left: vessel from which the measurements are taken. Upper right: the stack of interchangeable cores fit inside one larger steel cylinder. The varied amount of cores in the cylinder equate to different levels of pore volume from which the porosity can be calculated. Lower right: The stack of interchangeable cores. Lower left: angled view of cylinder and one of the steel cores.

Fig. F: Operation of the permeameter. The aluminum rod I am holding pushes the rock core into the vacuum chamber above. Pressure is set in the chamber and helium gas is shot upstream, measuring the flow rate (and subsequently, permeability) of a rock.

Fig. G: Various fossils that make up Indiana Limestone. From left to right: bryozoans, crinoids, and a crinoid stem. Photos courtesy of Michael Popp.

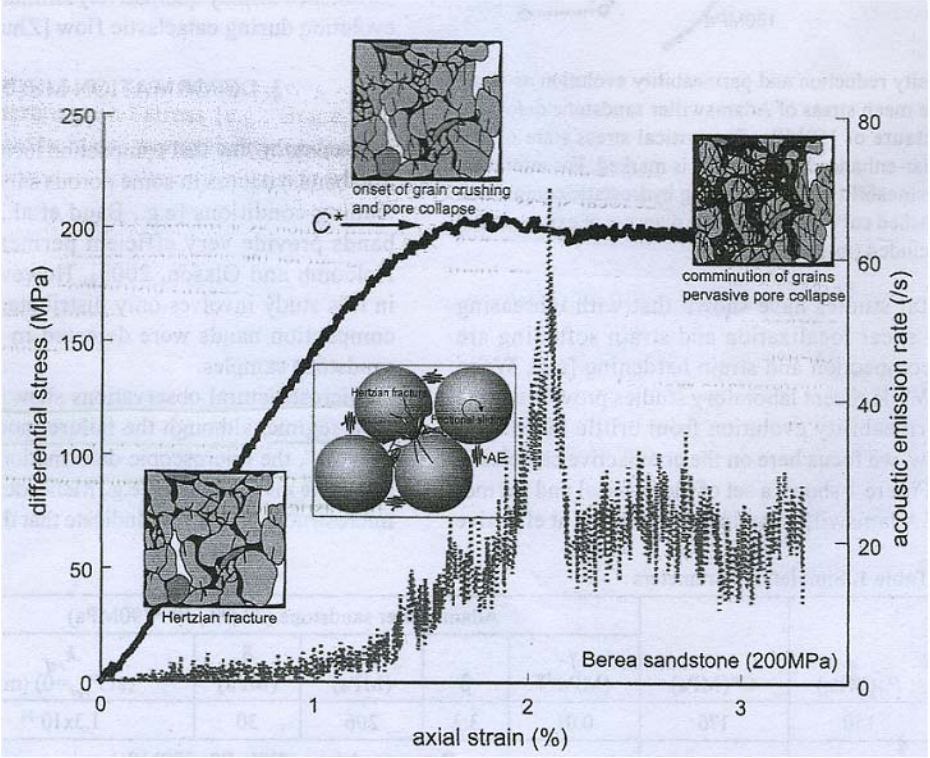

Fig. H: Differential stress vs. axial strain. Young's Modulus is calculated from this relationship, seen as the slope of the linear portion. Also plotted is the acoustic emission – axial strain relationship. Through this, one can determine when Hertzian fractures occur and at what intensity. (Zhu, 2006)

Appendix B: Stratigraphic Column

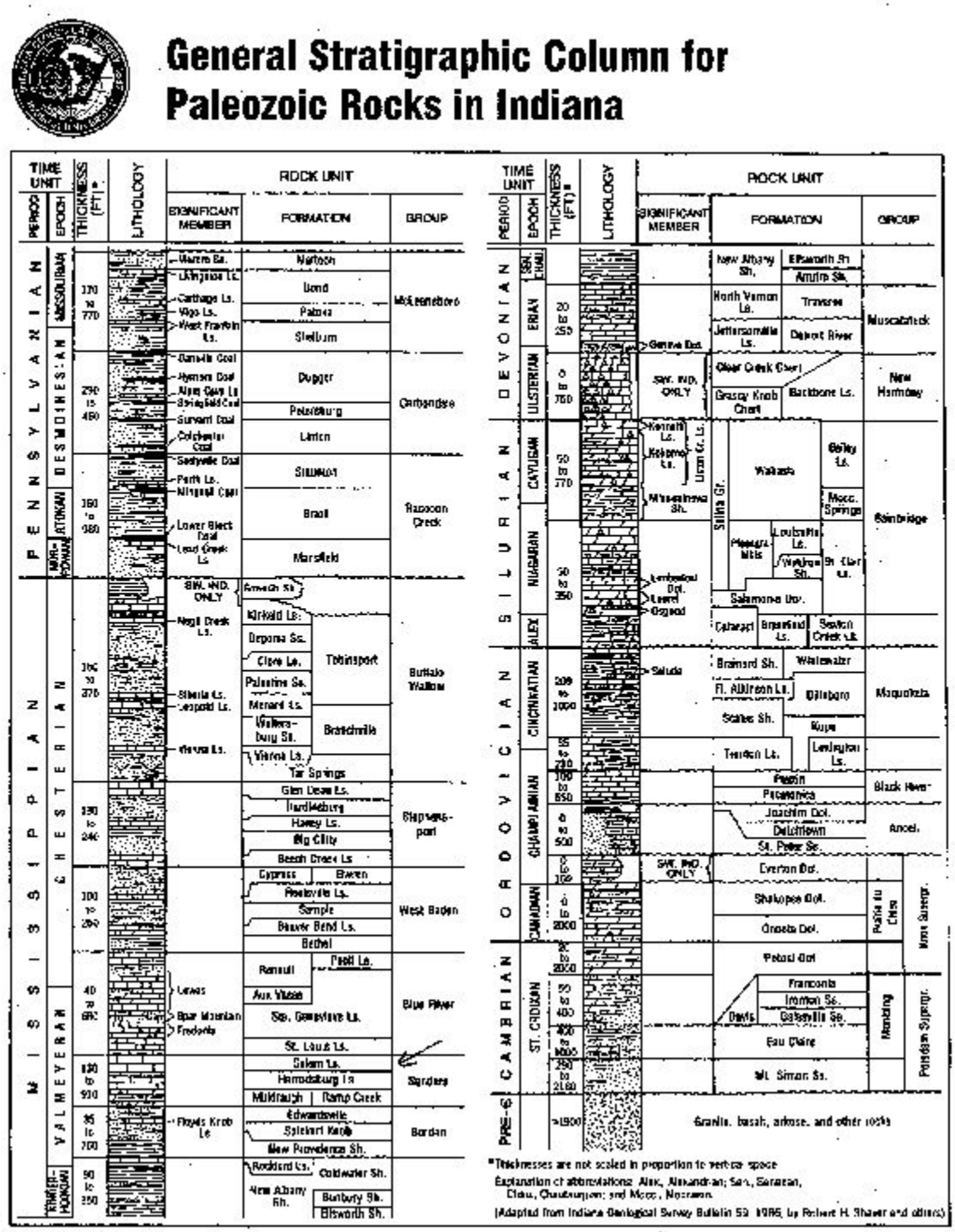

Appendix C: Raw Data, Velocity, and Permeability Reports: Core 3-11

Ultrasonic Velocity Measurement Report

Sample and Experiment Information for File IndianaLimestone3-11			
Well:		Organization:	NER
Depth:	0.0 m	Transducer:	vel_1in.hightemp
Formation:		Rock type:	
Dry bulk density:	2.270 gm/cm^3	Porosity:	
Sat. bulk density:	2.320 gm/cm^3	Pore fluids:	
Diameter:	25.40 mm	Entered Length:	50.80 mm

Comments:	User: lab on al1500-10f6 at Mon Apr 25 11:40:03 EDT 2011
Expt name:	IndianaLimestone3-11_50C_DL
Expt date:	Tue Apr 26 12:14:43 2011
Print date:	Wed Apr 27 08:21:39 2011
A2D File:	IndianaLimestone3-11.a2d

Observed Velocities and Moduli for File IndianaLimestone3-11									
Event	Conf	Pore	Diff	Temp	V_p	$V_s^{(1)}$	$V_s^{(2)}$	Young's Modulus	Poisson's Ratio
	MPa	MPa	MPa	°C	m/s	m/s	m/s	GPa	
0	13.7	9.9	5.4	22.6	3952	73667	27756	23901.50	1.003
3	13.7	9.9	6.4	48.8	3386	72151	28038	23314.50	1.002
6	20.7	9.9	6.1	49.5	3546	64597	27679	19783.80	1.003
10	20.7	10.0	29.6	48.2	3529	70565	27822	22486.60	1.003
14	20.6	9.9	23.8	47.5	3785	58028	28386	17357.80	1.004

Sample Lengths for File IndianaLimestone3-11	
Event	Sample Length
	mm
0	50.80
3	50.80
6	50.80
10	50.80
14	50.80

Waveform waterfall for **p** arrivals	
Experiment:	IndianaLimestone3-11_50C_DL
Well:	
Depth:	0
File name:	IndianaLimestone3-11

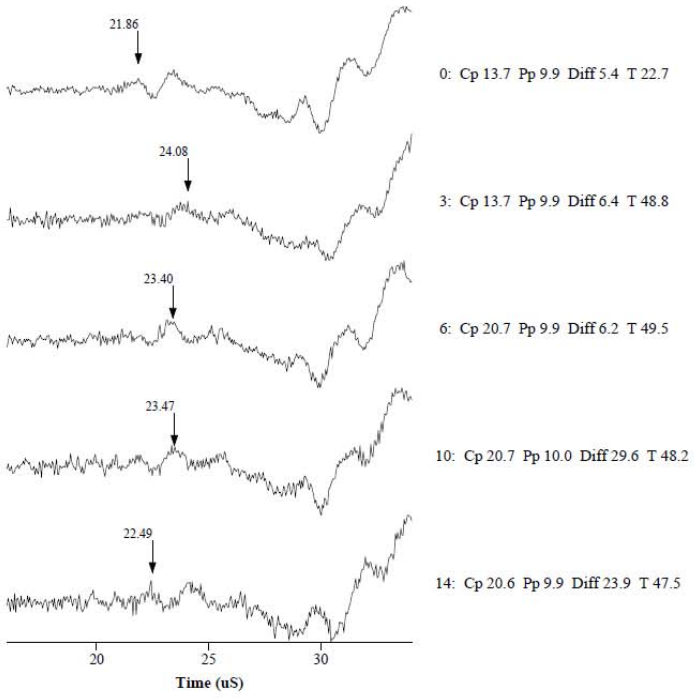

Waveform waterfall for **s1** arrivals	
Experiment:	IndianaLimestone3-11_50C_DL
Well:	
Depth:	0
File name:	IndianaLimestone3-11

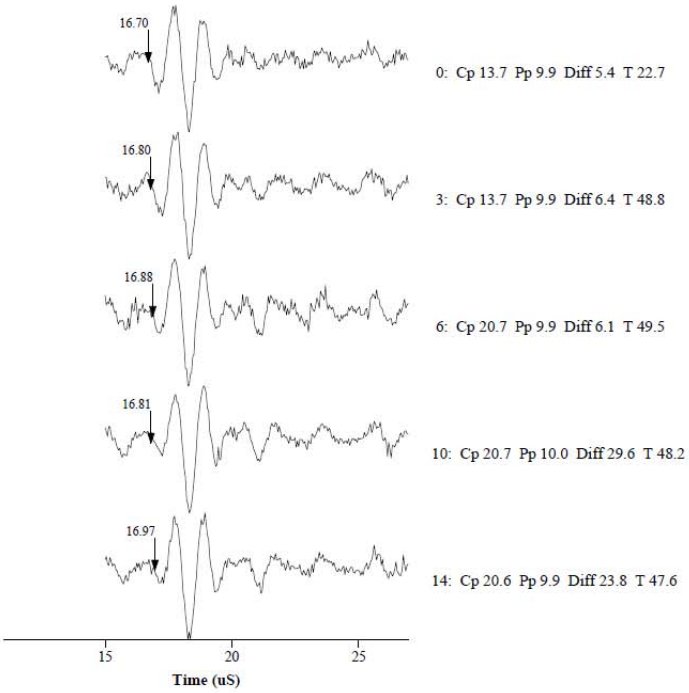

Waveform waterfall for **s2** arrivals	
Experiment:	IndianaLimestone3-11_50C_DL
Well:	
Depth:	0
File name:	IndianaLimestone3-11

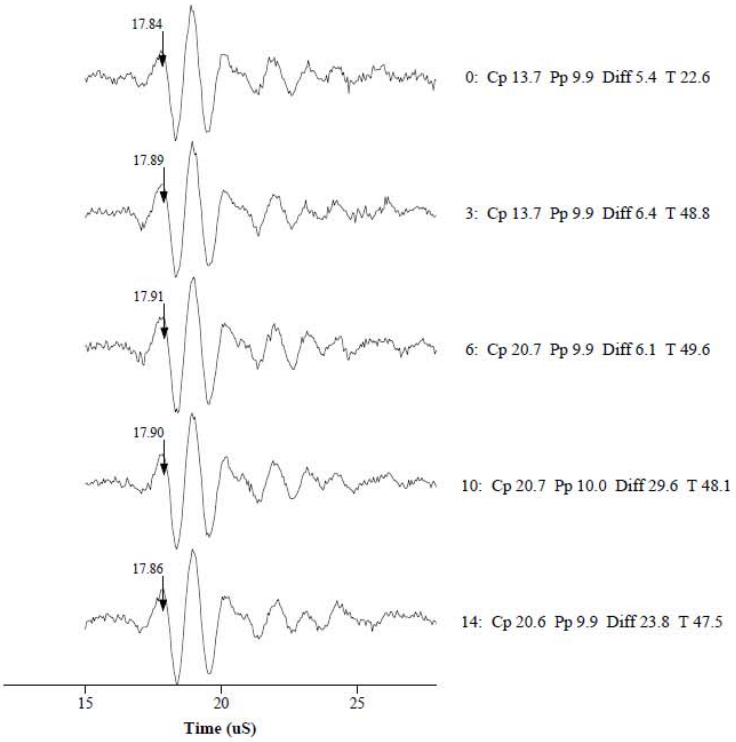

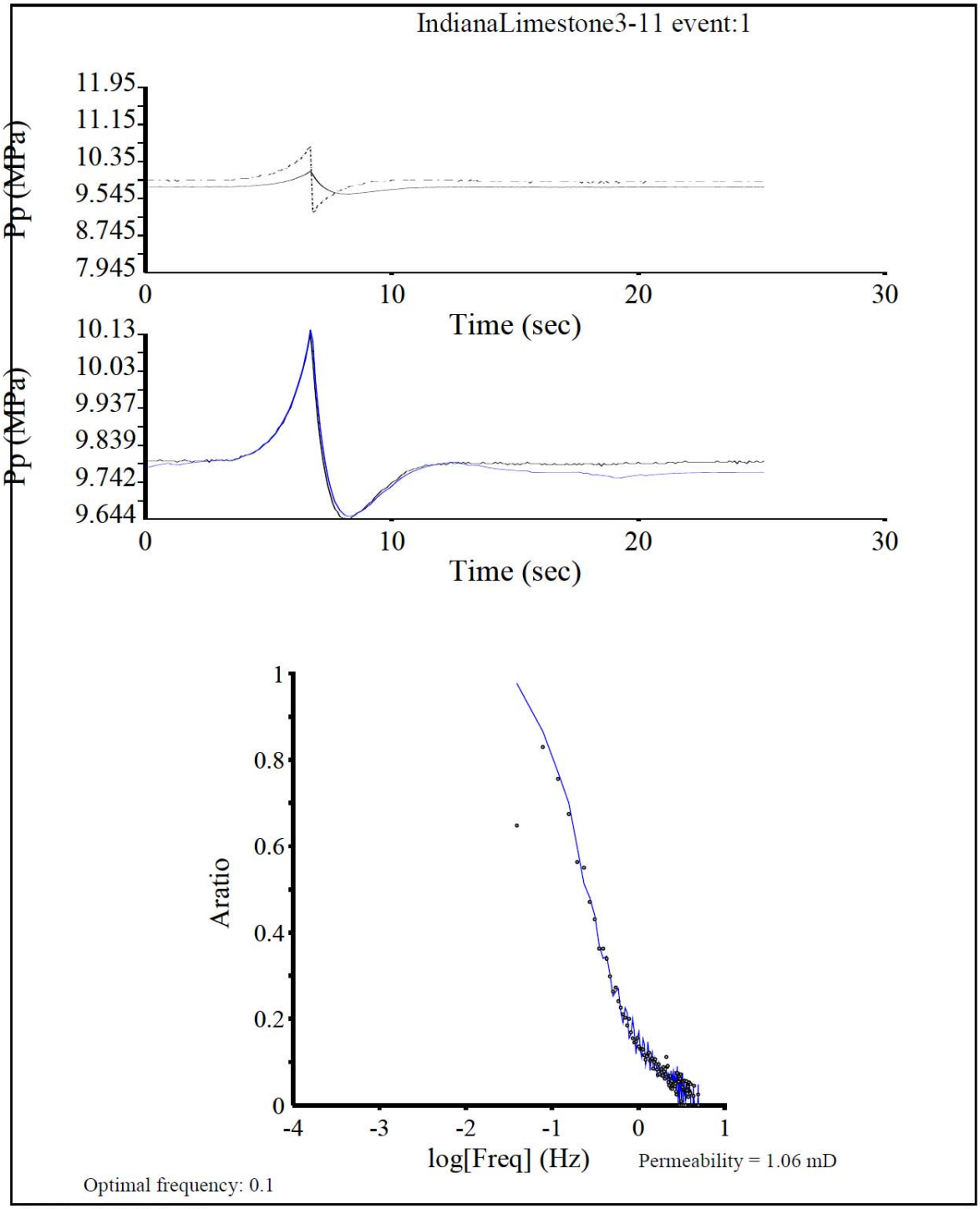
IndianaLimestone3-11 event:1
Pp (MPa)
11.95
11.15
10.35
9.545
8.745
7.945
0
10
20
30
Time (sec)
Pp (MPa)
10.13
10.03
9.937
9.839
9.742
9.644
0
10
20
30
Time (sec)
Aratio
1
0.8
0.6
0.4
0.2
0
-4
-3
-2
-1
0
1
log[Freq] (Hz)
Permeability = 1.06 mD
Optimal frequency: 0.1
Wed Apr 27 08:07:51 2011
NER

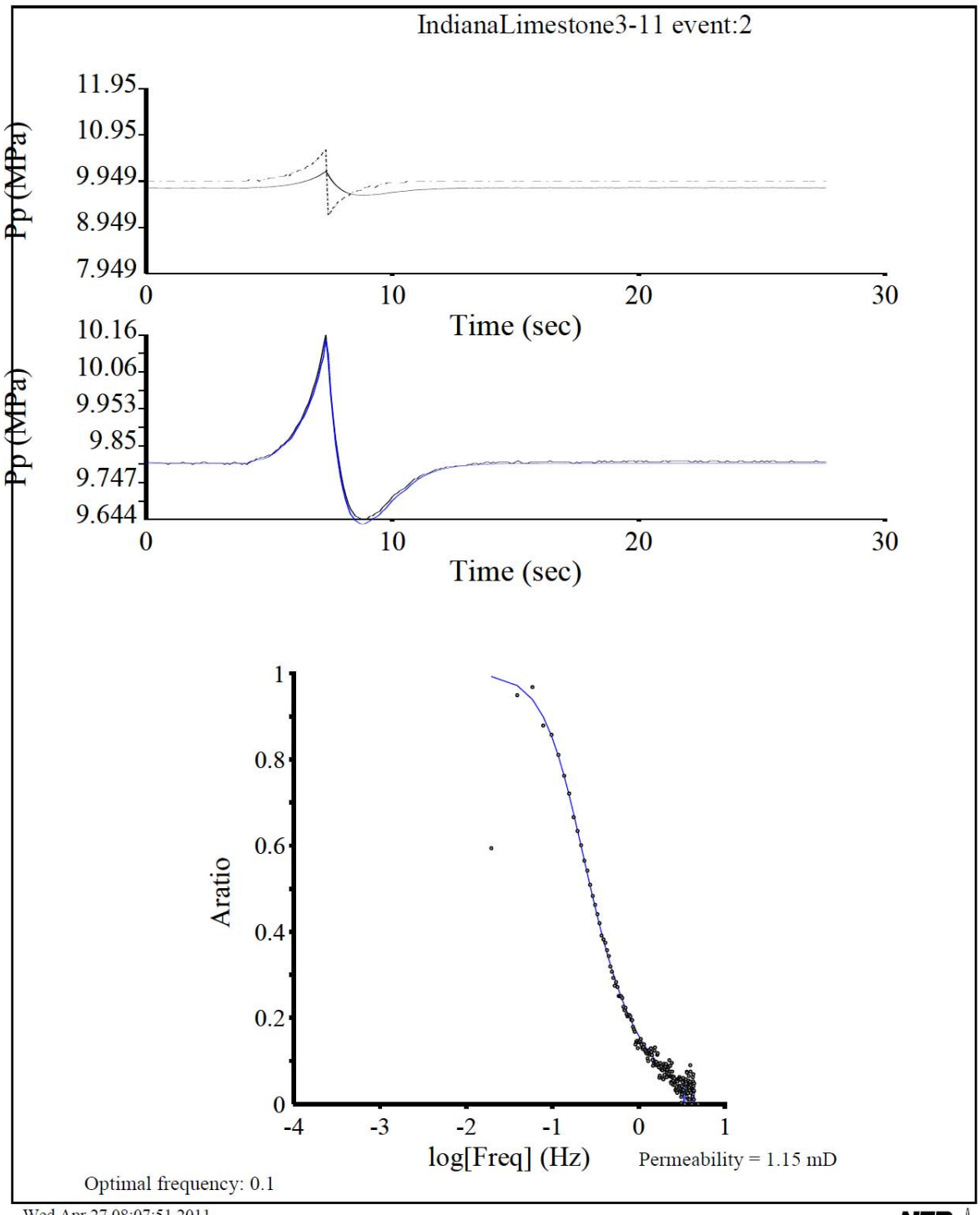
IndianaLimestone3-11 event:2
Pp (MPa)
11.95
10.95
9.949
8.949
7.949
0
10
20
30
Time (sec)
Pp (MPa)
10.16
10.06
9.953
9.85
9.747
9.644
0
10
20
30
Time (sec)
Aratio
1
0.8
0.6
0.4
0.2
0
-4
-3
-2
-1
0
1
log[Freq] (Hz)
Permeability = 1.15 mD
Optimal frequency: 0.1
Wed Apr 27 08:07:51 2011
NER

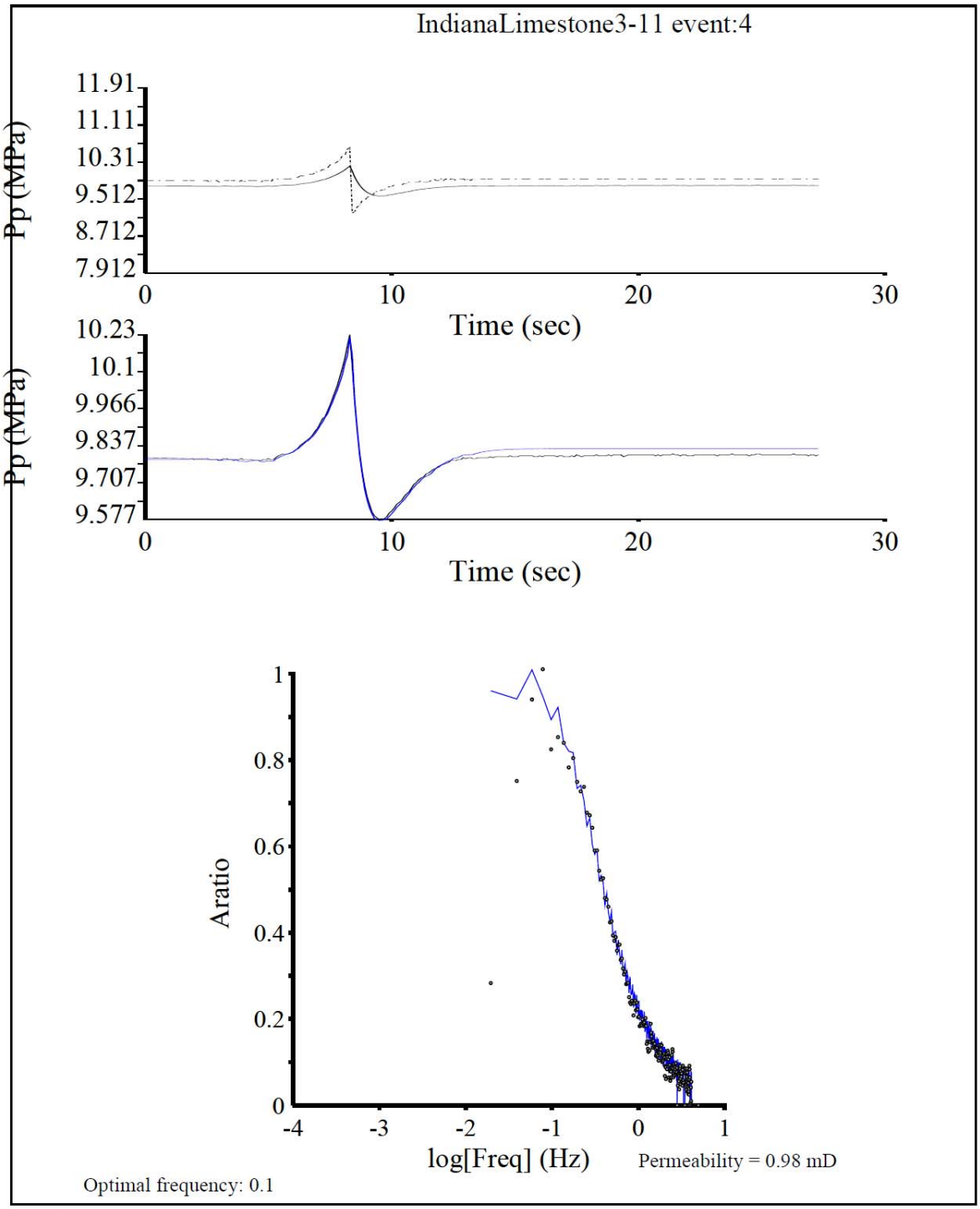
IndianaLimestone3-11 event:4
Pp (MPa)
11.91
11.11
10.31
9.512
8.712
7.912
0
10
20
30
Time (sec)
Pp (MPa)
10.23
10.1
9.966
9.837
9.707
9.577
0
10
20
30
Time (sec)
Aratio
1
0.8
0.6
0.4
0.2
0
-4
-3
-2
-1
0
1
log[Freq] (Hz)
Permeability = 0.98 mD
Optimal frequency: 0.1
Wed Apr 27 08:07:51 2011
NER

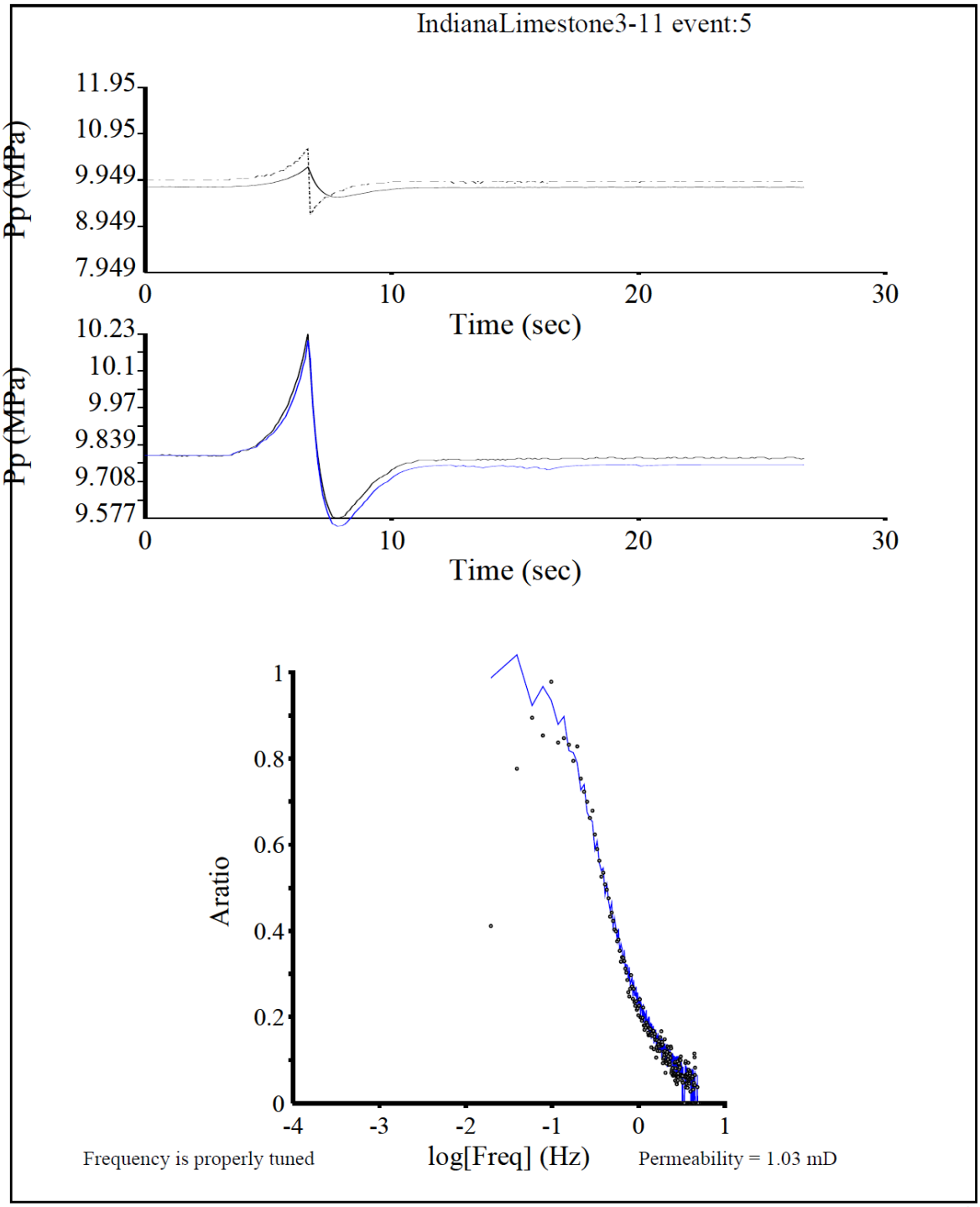
IndianaLimestone3-11 event:5
Pp (MPa)
11.95
10.95
9.949
8.949
7.949
0
10
20
30
Time (sec)
Pp (MPa)
10.23
10.1
9.97
9.839
9.708
9.577
0
10
20
30
Time (sec)
Aratio
1
0.8
0.6
0.4
0.2
0
-4
-3
-2
-1
0
1
log[Freq] (Hz)
Frequency is properly tuned
Permeability = 1.03 mD
Wed Apr 27 08:07:52 2011
NER

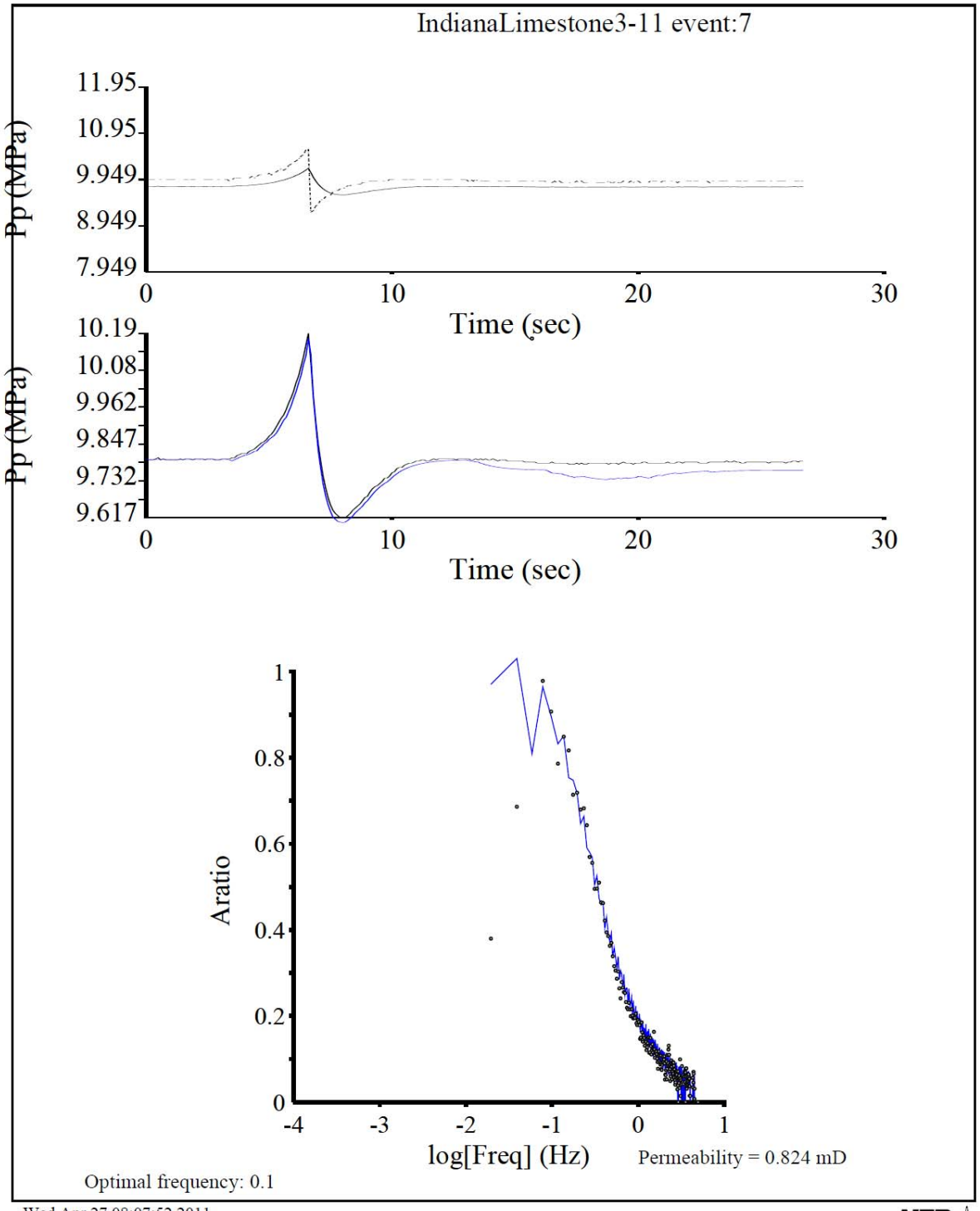
IndianaLimestone3-11 event:7
Pp (MPa)
11.95
10.95
9.949
8.949
7.949
0
10
20
30
Time (sec)
Pp (MPa)
10.19
10.08
9.962
9.847
9.732
9.617
0
10
20
30
Time (sec)
Aratio
1
0.8
0.6
0.4
0.2
0
-4
-3
-2
-1
0
1
log[Freq] (Hz)
Permeability = 0.824 mD
Optimal frequency: 0.1
Wed Apr 27 08:07:52 2011
NER

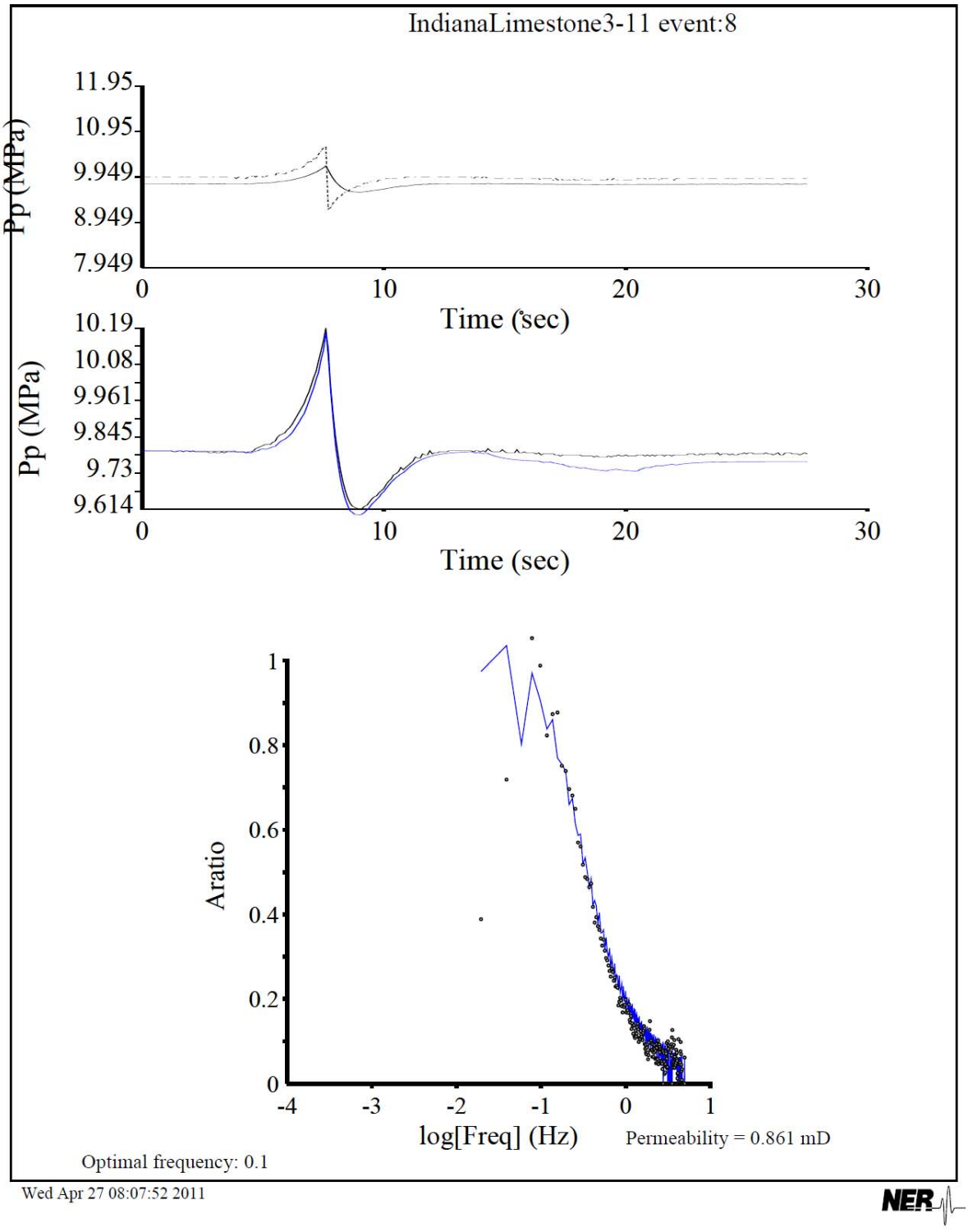
IndianaLimestone3-11 event:8
Pp (MPa)
11.95
10.95
9.949
8.949
7.949
0
10
20
30
Time (sec)
Pp (MPa)
10.19
10.08
9.961
9.845
9.73
9.614
0
10
20
30
Time (sec)
Aratio
1
0.8
0.6
0.4
0.2
0
-4
-3
-2
-1
0
1
log[Freq] (Hz)
Permeability = 0.861 mD
Optimal frequency: 0.1
Wed Apr 27 08:07:52 2011
NER

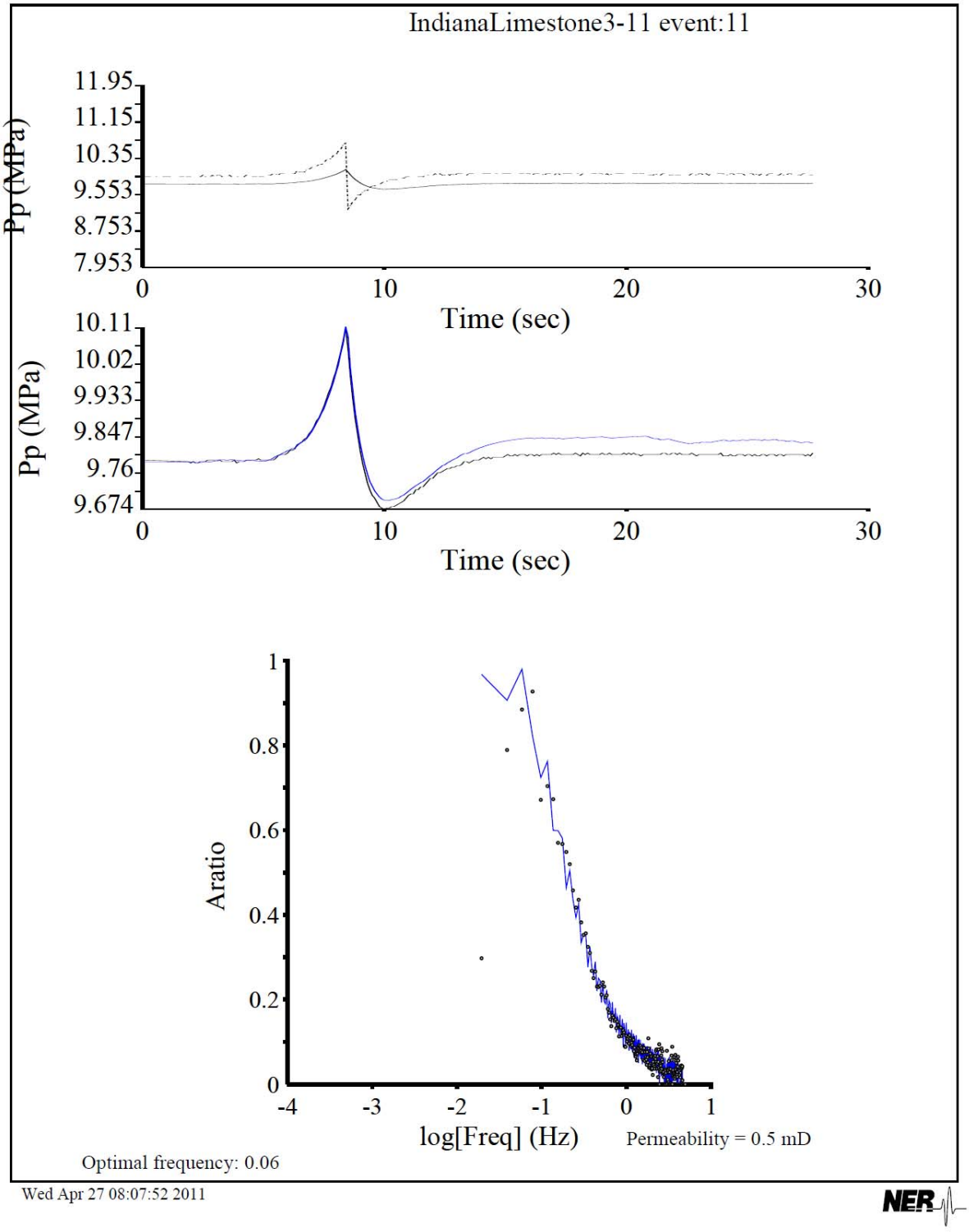
IndianaLimestone3-11 event:11
11.95
11.15
10.35
9.553
8.753
7.953
Pp (MPa)
0
10
20
30
Time (sec)
10.11
10.02
9.933
9.847
9.76
9.674
Pp (MPa)
0
10
20
30
Time (sec)
1
0.8
0.6
0.4
0.2
0
Aratio
-4
-3
-2
-1
0
1
log[Freq] (Hz)
Permeability = 0.5 mD
Optimal frequency: 0.06
Wed Apr 27 08:07:52 2011
NER

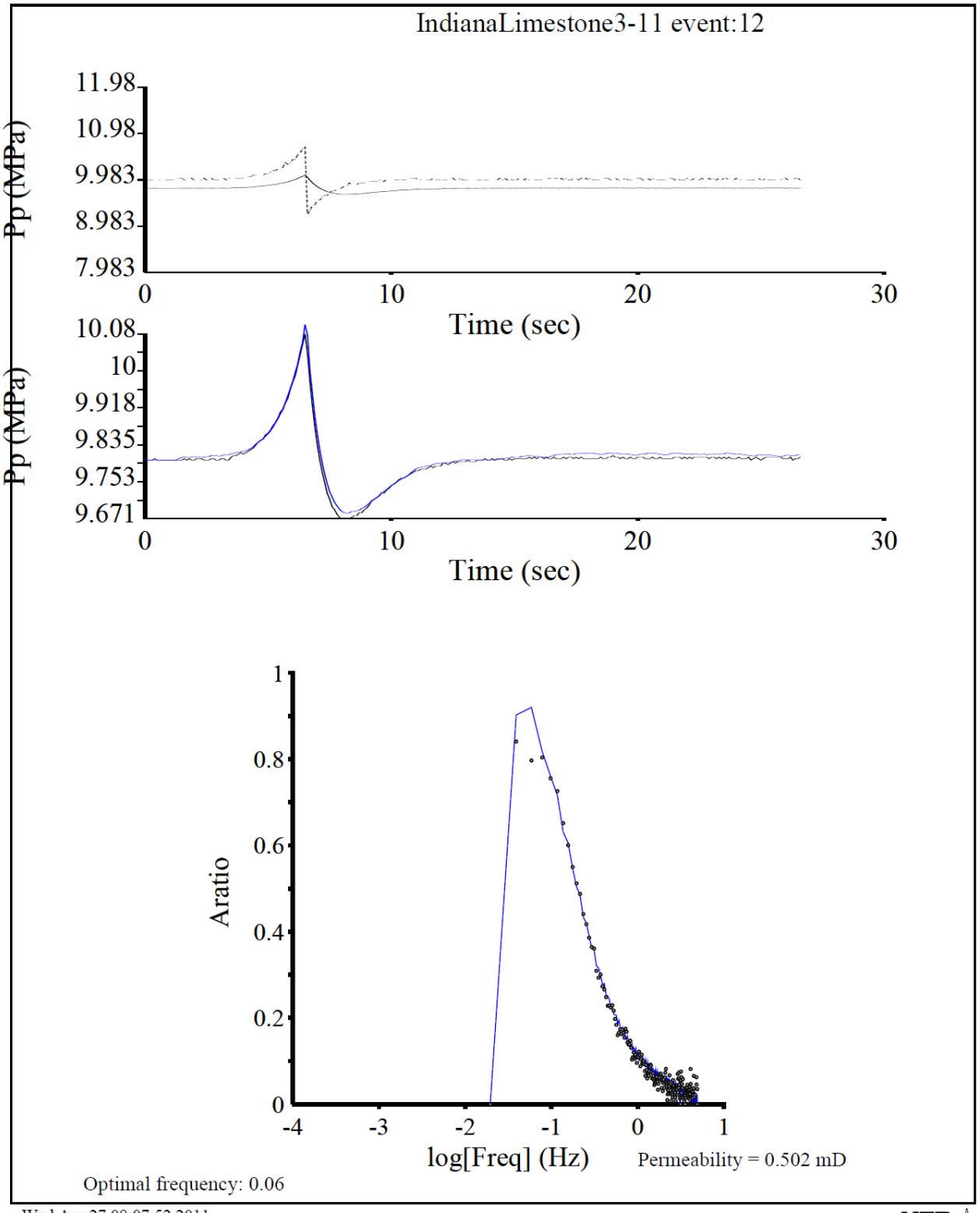
IndianaLimestone3-11 event:12
Pp (MPa)
11.98
10.98
9.983
8.983
7.983
0
10
20
30
Time (sec)
Pp (MPa)
10.08
10
9.918
9.835
9.753
9.671
0
10
20
30
Time (sec)
Aratio
1
0.8
0.6
0.4
0.2
0
-4
-3
-2
-1
0
1
log[Freq] (Hz)
Permeability = 0.502 mD
Optimal frequency: 0.06
Wed Apr 27 08:07:52 2011
NER

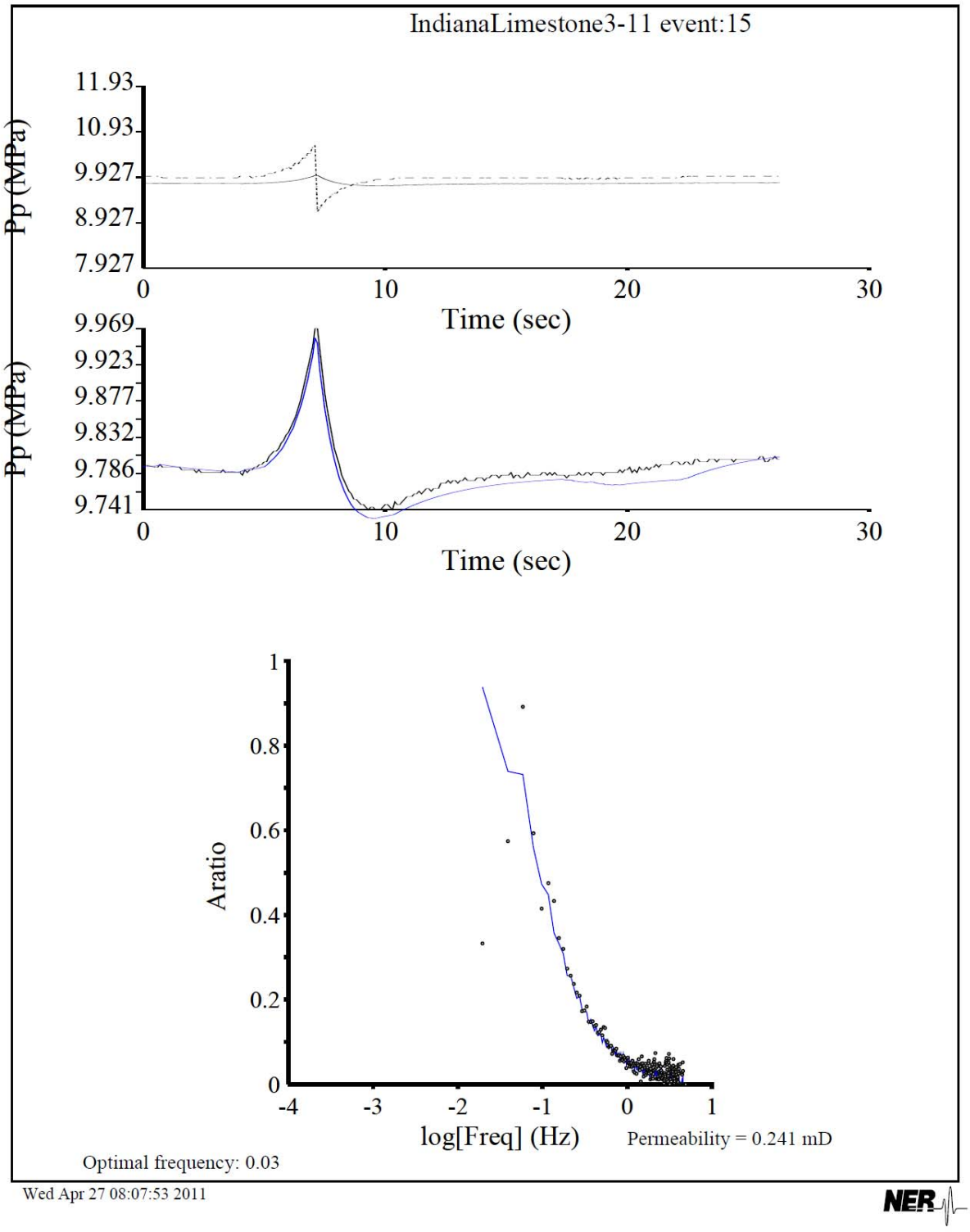
IndianaLimestone3-11 event:15
Pp (MPa)
11.93
10.93
9.927
8.927
7.927
0
10
20
30
Time (sec)
Pp (MPa)
9.969
9.923
9.877
9.832
9.786
9.741
0
10
20
30
Time (sec)
Aratio
1
0.8
0.6
0.4
0.2
0
-4
-3
-2
-1
0
1
log[Freq] (Hz)
Permeability = 0.241 mD
Optimal frequency: 0.03
Wed Apr 27 08:07:53 2011
NER

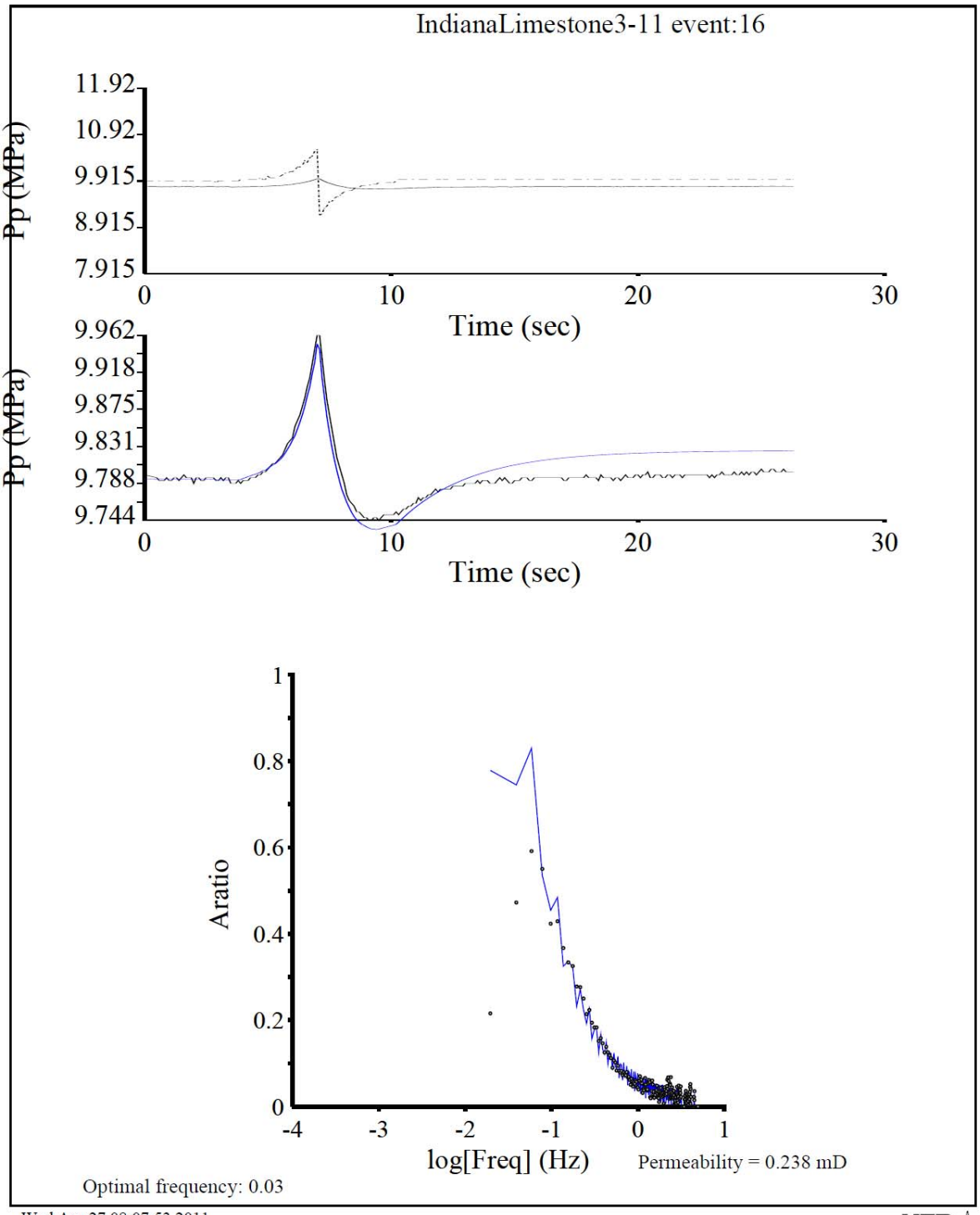
IndianaLimestone3-11 event:16
Pp (MPa)
11.92
10.92
9.915
8.915
7.915
0
10
20
30
Time (sec)
Pp (MPa)
9.962
9.918
9.875
9.831
9.788
9.744
0
10
20
30
Time (sec)
Aratio
1
0.8
0.6
0.4
0.2
0
-4
-3
-2
-1
0
1
log[Freq] (Hz)
Permeability = 0.238 mD
Optimal frequency: 0.03
Wed Apr 27 08:07:53 2011
NER

Permeability Measurement Report

Sample and Experiment Information for File IndianaLimestone3-11			
Well:		Organization:	NER
Depth:	0.0 m	Core Holder:	Vol_Out
Formation:		Rock type:	
Dry bulk density:	2.27	Porosity:	
Sat. bulk density:	2.32	Pore fluids:	
Diameter:	25.40 mm	Entered Length:	50.80 mm

Comments: User: lab on al1500-10f6 at Mon Apr 25 11:40:03 EDT 2011
Expt name: IndianaLimestone3-11_50C_DL
Expt date: Tue Apr 26 12:14:43 2011
Print date: Wed Apr 27 08:21:02 2011
A2D File: IndianaLimestone3-11.a2d

Permeability and Specific Storage for File IndianaLimestone3-11							
Event	Type	Conf	Pore Top	Diff	Temp	Perm	Storage
		MPa	MPa	MPa	°C	μD	m^{-1}
1	aspike	13.7	9.9	5.4	22.7	1.06e+03	0.00
2	aspike	13.8	9.9	5.6	23.0	1.15e+03	0.00
4	aspike	13.8	9.9	6.4	48.9	980.	0.00
5	aspike	13.7	9.9	6.4	48.9	1.03e+03	0.00
7	aspike	20.7	9.9	6.1	49.5	824.	0.00
8	aspike	20.7	9.9	6.1	49.3	861.	0.00
11	aspike	20.7	10.0	29.6	48.1	500.	0.00
12	aspike	20.7	10.0	29.5	48.1	502.	0.00
15	aspike	20.7	9.9	23.4	47.4	241.	0.00
16	aspike	20.7	9.9	23.2	47.4	238.	0.00

Sample Lengths for File IndianaLimestone3-11	
Event	Sample Length
	mm
1	50.80
2	50.80
4	50.80
5	50.80
7	50.80

Sample Lengths for File IndianaLimestone3-11	
Event	Sample Length
8	50.80
11	50.80
12	50.80
15	50.80
16	50.80

Appendix D: Additional Thin Section Photos and Photomicrographs

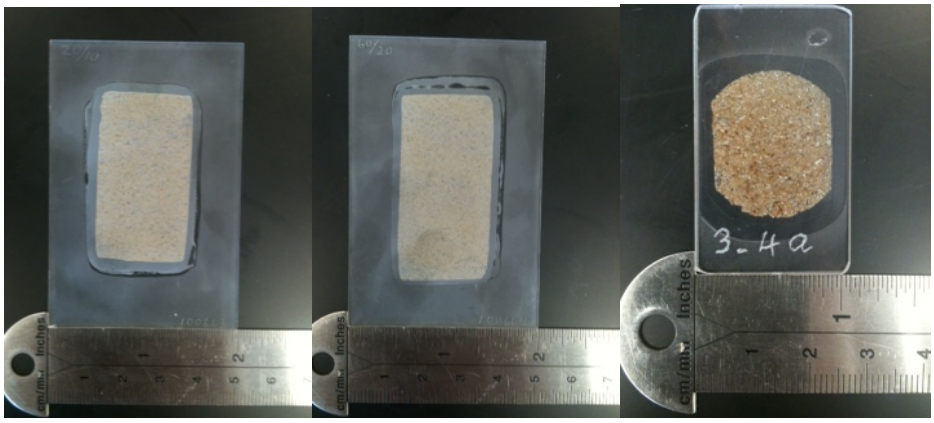

D.1: Left: Thin section of triaxial experiment at effective pressure 10 MPa. Middle: Triaxial experiment at effective pressure 50 MPa. Right: Undeformed core. Twin and microcrack density counts are documented.

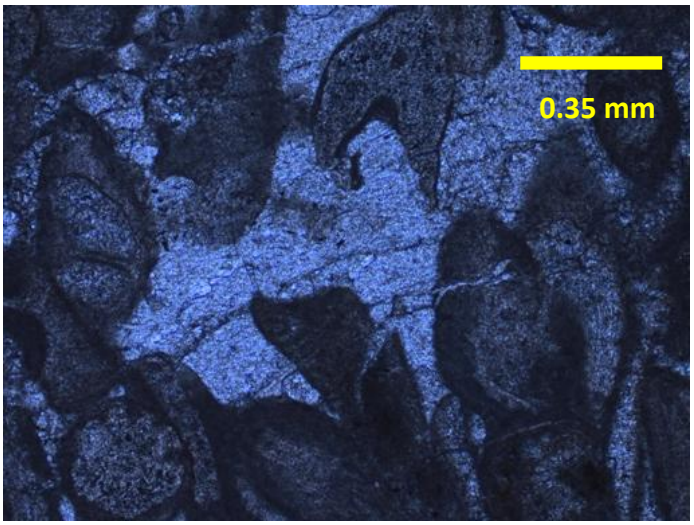

D.2:Transgranular crack, zone 3, effective pressure 10 MPa.

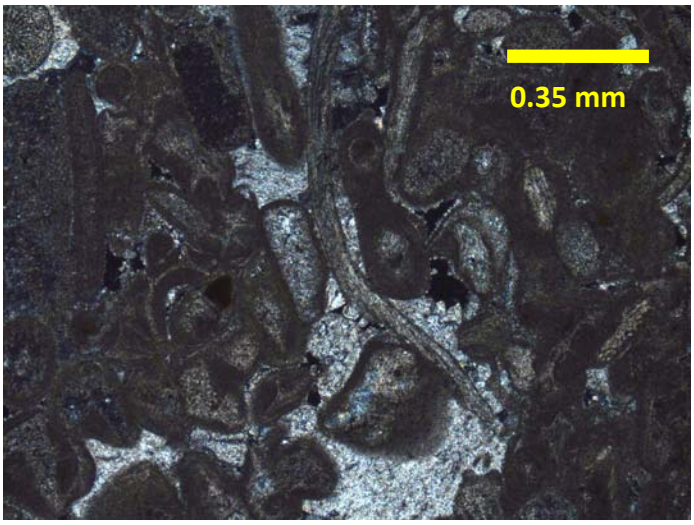

Overall view, effective pressure 10 MPa.

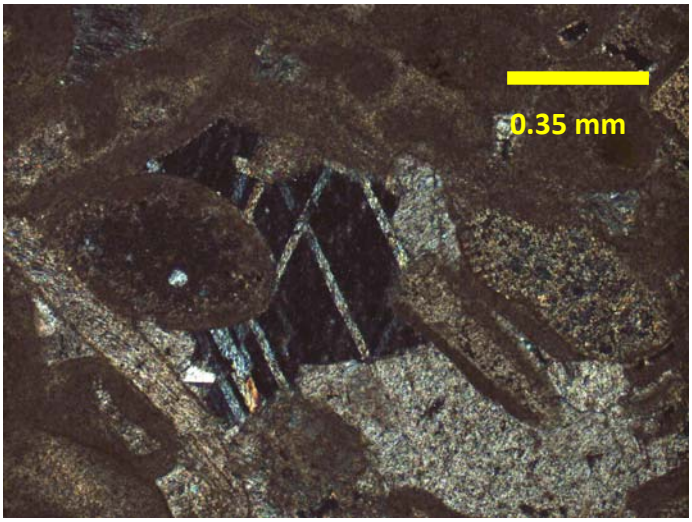

Twinning, effective pressure 10 MPa.

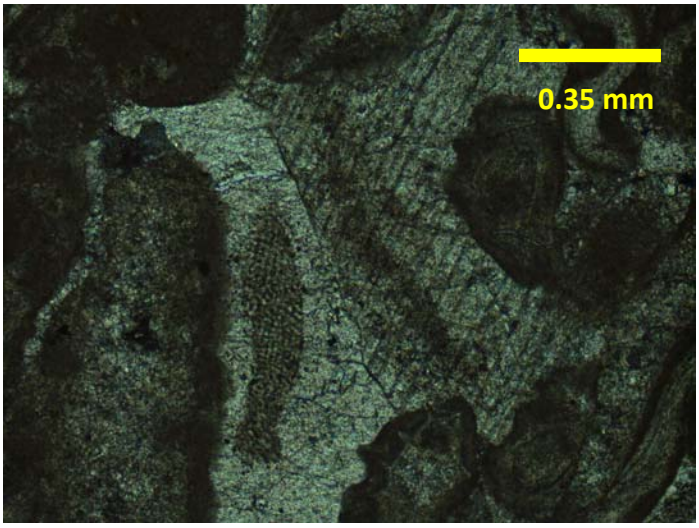

Cracks & twinning, effective pressure 10 MPa.

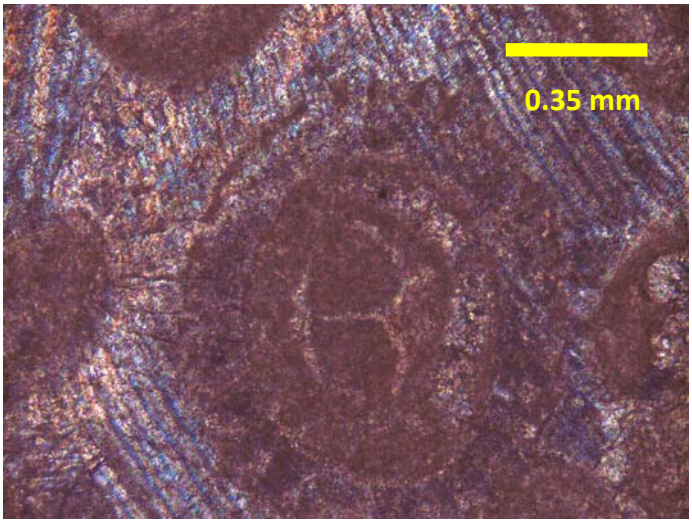

Grain cracks into fossil, effective pressure 50 MPa.

Appendix E: Honor Code

I pledge on my honor that I have not given or received any unauthorized assistance or plagiarized on this assignment.

Katherine Watter